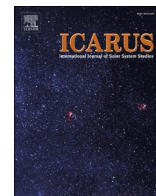




Since January 2020 Elsevier has created a COVID-19 resource centre with free information in English and Mandarin on the novel coronavirus COVID-19. The COVID-19 resource centre is hosted on Elsevier Connect, the company's public news and information website.

Elsevier hereby grants permission to make all its COVID-19-related research that is available on the COVID-19 resource centre - including this research content - immediately available in PubMed Central and other publicly funded repositories, such as the WHO COVID database with rights for unrestricted research re-use and analyses in any form or by any means with acknowledgement of the original source. These permissions are granted for free by Elsevier for as long as the COVID-19 resource centre remains active.



# Atmospheric response to high-resolution topographical and radiative forcings in a general circulation model of Venus: Time-mean structures of waves and variances

Masaru Yamamoto<sup>a,\*</sup>, Kohei Ikeda<sup>b</sup>, Masaaki Takahashi<sup>b,c</sup>

<sup>a</sup> Research Institute for Applied Mechanics, Kyushu University, Kasuga, Fukuoka 816-8580, Japan

<sup>b</sup> National Institute for Environmental Studies, Tsukuba, Ibaraki 305-8506, Japan

<sup>c</sup> Atmosphere and Ocean Research Institute, The University of Tokyo, Kashiwa, Chiba 277-8564, Japan

## ABSTRACT

Thermal tides, stationary waves, and general circulation are investigated using a T63 Venus general circulation model (GCM) with solar and thermal radiative transfer in the presence of high-resolution surface topography, based on time average analysis. The simulated wind and static stability are very similar to the observed ones (e.g., Horinouchi et al., 2018; Ando et al., 2020). The simulated thermal tides accelerate an equatorial superrotational flow with a speed of  $\sim 90 \text{ m s}^{-1}$  around the cloud-heating maximum ( $\sim 65 \text{ km}$ ). The zonal-flow acceleration rates of  $0.2\text{--}0.5 \text{ m s}^{-1} \text{ Earth day}^{-1}$  are produced by both horizontal and vertical momentum fluxes at low latitudes. In the GCM simulation, strong solar heating above the cloud top ( $>69 \text{ km}$ ) and infrared heating around the cloud bottom ( $\sim 50 \text{ km}$ ) modify the vertical structures of thermal tides and their vertical momentum fluxes, which accelerate zonal flow at  $10^3 \text{ Pa}$  ( $\sim 75 \text{ km}$ ) and  $10^4 \text{ Pa}$  ( $\sim 65 \text{ km}$ ) at the equator and around  $10^3 \text{ Pa}$  at high latitudes.

Below and in the cloud layer, surface topography weakens the zonal-mean zonal flow over the Aphrodite Terra and Maxwell Montes, whereas it enhances the zonal flow in the southern polar region. The high-resolution topography produces stationary fine-scale bow structures at the cloud top and locally modifies the variances in the geographical coordinates (i.e., the activity of unsteady wave components). Over the high mountains, vertical spikes of the vertical wind variance are found, indicating penetrative plumes and gravity waves. Negative momentum flux is also locally enhanced at the cloud top over the equatorial high mountains. In the solar-fixed coordinate system, the variances (i.e., the activity of waves other than thermal tides) of flow are relatively higher on the nightside than on the dayside at the cloud top. Strong dependences of the eddy heat and momentum fluxes on local time are predominant. The local-time variation of the vertical eddy momentum flux is produced by both thermal tides and solar-related, small-scale gravity waves.

## 1. Introduction

On Venus, thermal tides dominate the middle atmosphere between 40 and 90 km (Schofield and Taylor, 1983; Pechmann and Ingersoll, 1984; Zasova et al., 2002, 2007; Tellmann et al., 2009; Grassi et al., 2010; Scarica et al., 2019; Ando et al., 2018; Kouyama et al., 2019). They propagate vertically and have a strong day-to-night circulation at 65–70 km. The thermal tides simulated in general circulation models (GCMs) were compared with the observations (e.g., Scarica et al., 2019; Takagi et al., 2018; Yamamoto et al., 2019). According to Ignatiev et al. (2009), the cloud-top altitude has latitude dependence and the range of 63–74 km. The average value ( $69 \text{ km}$ ,  $\sim 4.54 \times 10^3 \text{ Pa}$ ) is considered as the cloud top under the condition of globally uniform clouds assumed in our GCM.

Vertically propagating tides induce superrotation around the cloud-heating maximum ( $\sim 65 \text{ km}$ ,  $9.75 \times 10^3 \text{ Pa}$ , Ikeda, (2011); Yamamoto

et al., 2019), which corresponds to the heating maximum around the cloud top in the low-UV model of Crisp (1986). The superrotation mechanism associated with the vertical propagation of the tides has been fully investigated (e.g., Fels and Lindzen, 1974; Newman and Leovy, 1992; Takagi and Matsuda, 2007; Sánchez-Lavega et al., 2017). In several theoretical studies of thermal tides (Fels and Lindzen, 1974; Takagi et al., 2018), however, strong solar heating above the cloud top ( $>69 \text{ km}$ ,  $\text{CO}_2$  absorption at  $2.7$  and  $4.3 \mu\text{m}$ ) and infrared (IR) heating around the cloud bottom ( $\sim 50 \text{ km}$ ,  $\sim 10^5 \text{ Pa}$ ) were not taken into account. They are required for accurate simulation of the thermal tides. Thus, we need to investigate the thermal tides using a general circulation model (GCM) with radiative transfer code, based on the same approach as Lebonnois et al., (2010), Ikeda (2011), and Mendonça and Read (2016) different from simplified models with an assumed solar heating rate and Newtonian cooling. In addition to the conventional theory of vertically propagating thermal tides, Yamamoto and

\* Corresponding author.

E-mail address: [yamakatu@kyudai.jp](mailto:yamakatu@kyudai.jp) (M. Yamamoto).

<https://doi.org/10.1016/j.icarus.2020.114154>

Received 23 March 2020; Received in revised form 28 September 2020; Accepted 5 October 2020

Available online 9 October 2020

0019-1035/© 2020 The Authors.

Published by Elsevier Inc.

This is an open access article under the CC BY-NC-ND license

(<http://creativecommons.org/licenses/by-nc-nd/4.0/>).



Takahashi (2004, 2006) found thermal tides produce equatorward momentum flux, which contributes to the maintenance of the cloud-top superrotation (Horinouchi et al., 2020). Thus, we must investigate both the eddy vertical and horizontal momentum fluxes of thermal tides.

Recent satellite-based observations have shown a conspicuous variation of the zonal flow (Bertaux et al., 2016) and global-scale stationary bow-shaped waves (Fukuhara et al., 2017) over the Aphrodite Terra. GCM simulations with topography have been conducted in previous works (Herrnstein and Dowling, 2007; Yamamoto and Takahashi, 2009; Lebonnois et al., 2010, 2018; Navarro et al., 2018; Yamamoto et al., 2019). As reviewed in Sánchez-Lavega et al. (2017), the effects of Venus' surface topography on superrotation vary considerably with model. In Herrnstein and Dowling (2007), the presence of the topography in their GCM leads to the slowness of the maximum zonal wind (which is 20 m s<sup>-1</sup> slower than that under the flat-surface condition) and a latitudinal asymmetry of the zonal flow (which differs by ~10 m s<sup>-1</sup> between the Northern and Southern Hemispheres). In contrast, Lebonnois et al. (2010) showed an increase in the superrotation and no significant asymmetry in the presence of the topography. In the T21 AGCMs of Yamamoto and Takahashi (2009) and Yamamoto et al. (2019), the topography slightly weakens the superrotation and does not produce a significantly asymmetric structure in the general circulation. At the present stage, the effects of high-resolution topography on the dynamics (e.g., general circulation, longitudinal wind variation, and the global-scale bow-shaped wave) have not been fully understood.

To model the general circulation of Venus more realistically, simplified Newtonian cooling has been replaced by infrared radiative transfer code (Eymet et al., 2009) in GCMs of Venus (Lebonnois et al., 2010, 2016; Garate-Lopez and Lebonnois, 2018). Mendonça and Read (2016) developed the Oxford Planetary Unified Model System for Venus using a radiative transfer model (Mendonça et al., 2015), in which both solar and thermal radiation are taken into account in the two-stream code. Ikeda (2011) developed a radiative transfer model for Venus' solar and thermal radiation using two-stream discrete ordinate and *k*-distribution methods in a GCM developed at the Atmosphere and Ocean Research Institute (AORI) of the University of Tokyo and diagnosed strong solar heating above the cloud top and infrared heating at the cloud bottom. Using Ikeda's GCM, Yamamoto et al. (2019) simulated the indirect circulation formed by the thermal tide and baroclinic waves around the jets, topographical modification of middle-atmospheric structure, and cloud-top wind fields that are similar to the subsolar zonal wind speed minimum and strong poleward flows observed by Akatsuki UV cloud tracking (Yamazaki et al., 2018; Horinouchi et al., 2018). However, although the solar-locked circulation was discussed in Yamamoto et al. (2019), the three-dimensional structure of diurnal and semidiurnal tides induced by realistic radiative forcing was not investigated. In addition, the momentum fluxes and their zonal-flow acceleration of stationary waves forced by high-resolution surface topography were not accurately estimated in Yamamoto et al. (2019), because of the low horizontal resolution (T21) of the model.

Differing from our previous work, the present work decomposes the solar-locked atmospheric structure into diurnal and semidiurnal tides, because diurnal and semidiurnal temperature structures have been seen in IR observations (Schofield and Taylor, 1983; Pechmann and Ingersol, 1984; Kouyama et al., 2019). In our current Venus GCM that includes radiative transfer processes, the increase of the horizontal resolution (T21 to T63) greatly improves the effect of the topography on general circulation and stationary waves. Moreover, we also expect that the sharpness of streaks in the cloud layer (e.g., Kashimura et al., 2019) will be improved in the high-resolution model. The present work investigates stationary and solar-locked components of the streaks. In general, it is difficult to estimate the zonal-mean eddy heat and momentum fluxes from single satellite observations limited to either the day-side or night-side. As was discussed in Yamamoto et al. (2019), because the dayside averages of the fluxes are not the same as the zonal averages over the whole longitude range, the longitudinal variations of the eddy heat and

momentum fluxes should also be carefully investigated. Our purpose in this work is to better evaluate the three-dimensional structure and momentum transport of thermal tides and stationary waves induced by realistic topographical and radiative forcing. The model evaluation of these waves must be compared with recently updated observations and modeling. Further, we discuss the dynamical impacts of a high-resolution model on the general circulation and the local-time and geographical distributions of eddy activity and their heat and momentum fluxes, based on time average analyses of meteorological elements.

## 2. Model and data analysis

### 2.1. Model description

The model used is the same as the Venus GCM of Yamamoto et al. (2019), except for the horizontal resolution and its related parameters. In this model, a radiative transfer model with 28 bands for a Venus GCM using two-stream discrete ordinate and *k*-distribution methods is implemented (Ikeda, 2011). The base model is the Center of Climate System Research/National Institute for Environmental Studies AGCM (Numaguti et al., 1997) and the Venusian model was developed at the AORI of the University of Tokyo (Ikeda, 2011). The model atmosphere from the surface to ~95 km has 52 vertical levels (L52) in sigma coordinates ( $\sigma = P/P_s$ , where  $P_s$  is the surface pressure). The truncation wavenumber is 63 (T63) in our spectral model, giving a horizontal resolution three-times finer than that in the T21 model in Yamamoto et al. (2019). The physical processes are calculated on 96 (latitude) × 192 (longitude) grids.

The physical parameters are listed in Table 1. Parameterization of zonal flow deceleration by subgrid-scale gravity waves is simplified by Rayleigh friction around the top boundary. The coefficient  $\alpha_R$  is defined as

$$\alpha_R = \{1 + \tanh[(z - z_{TOP})/(10 \text{ km})]\}/(240 \text{ h}), \quad (1)$$

where  $z = -(5 \text{ km}) \ln \sigma$  and  $z_{TOP} = -(5 \text{ km}) \ln \sigma_{TOP}$  using the uppermost-level sigma  $\sigma_{TOP} (= 6.60 \times 10^{-7})$ . The *e*-folding time constant of the fourth-order horizontal diffusion for the maximum wavenumber is 12 h, where h is earth hours. This value is half the default value used in a T42 AGCM (K1-developer, 2004). Yamamoto and Takahashi (2007) reported that the zonal-mean structure is not greatly modified by the very small axis tilt of the planetary rotation, though long-period variations of the zonal flow are seen in their model. Thus, the seasonal variation is not considered. The T63 simulation in the present work was restarted from the same initial conditions as those in the nudging-free restart run of Yamamoto et al. (2019). The initial conditions in the restart run were calculated from the quasi-equilibrium state at Venus day 90 in the nudging T21 run of Yamamoto et al. (2019).

**Table 1**  
Physical and model parameters.

Parameter (Symbol)	Value
Planetary rotation period ( $2\pi/\Omega$ )	243 Earth days
Solar day	117 Earth days
Planetary radius ( <i>r</i> )	6051.848 km
Axial tilt	0°
Gravitational acceleration ( <i>g</i> )	8.87 m s <sup>-2</sup>
Standard surface pressure ( $P_{STD}$ )	$9.21 \times 10^4$ hPa
Solar constant ( <i>S</i> )	2607 W m <sup>-2</sup>
Gas constant ( <i>R</i> )	191.4 J kg <sup>-1</sup> K <sup>-1</sup>
Specific heat at constant pressure ( $C_p$ )	$9 \times 10^2$ J kg <sup>-1</sup> K <sup>-1</sup>
Drag coefficient ( $C_D$ )	$4 \times 10^{-3}$
The coefficient for vertical diffusion	0.8 m <sup>2</sup> s <sup>-1</sup>
The <i>e</i> -folding time constant of horizontal diffusion for maximum wavenumber	12 h

by interpolating them to the T63L52 grid points (96 (latitude)  $\times$  192 (longitude)  $\times$  52 layers) in the present work. Although the model domain covers  $\sim 95$  km, the strong Rayleigh friction acts as the sponge layer around the top boundary. In the analysis, we investigated the region below the  $10^2$ -Pa altitude ( $\sim 86$  km).

Magellan topographic data (Ford and Pettengill, 1992) were used to specify terrain height at the lower boundary in a control experiment with topography (Topo). The output data of the Topo was investigated in the present work. For comparison with the Topo, a flat surface experiment without the topography (Flat) was also investigated (see Section 3.4).

## 2.2. Data analysis

In the T63 run restarted from Venus day 90 of Yamamoto et al. (2019), the model results show a quasi-equilibrium state on Venus day 100 and 101 (Venus day 10 and 11 from the restart, Fig. A1b in Appendix A). We analyzed output data obtained during the two Venus days at 3-h intervals. An example of output data for 10 to 100 earth days on Venus day 10 from the restart (Hovmöller diagram of vertical wind velocity at the equatorial cloud top in geographical coordinates) is shown as Fig. A2a. The general circulation and waves are investigated

based on time averages of the meteorological elements ( $X$ ) in geographical and solar-fixed coordinate systems. Longitude in the geographical coordinate is topographically fixed and expressed in degrees from 0 to  $360^\circ$  (Fig. 1a of Yamamoto et al., 2019). The super-rotational wind flows from east ( $0^\circ$ ) to west ( $360^\circ$ ) in the longitudinal direction. The solar-fixed coordinate frame rotates around the planet with a period of 117 Earth days in the geographical coordinate frame. Longitude in the solar-fixed coordinates is expressed by local time (e.g., the subsolar longitude is defined as 12 LT and the antisolar longitude as 0 LT and 24 LT).

The time averages are defined as follows:

$$X_G^{TM} = \frac{1}{N} \sum_{n=1}^{n=N} X_G(t = ndt), \quad (2)$$

$$X_S^{TM} = \frac{1}{N} \sum_{n=1}^{n=N} X_S(t = ndt), \quad (3)$$

where superscript “TM” (time mean) indicates the average over the total number of time steps  $N$  ( $= 1872$ ),  $\sum$  is the sum of  $X(t = ndt)$  from  $n = 1$  to  $n = N$ ,  $dt$  is the time increment (3 h). Subscripts “G” and “S” mean meteorological elements in the geographical and solar-fixed

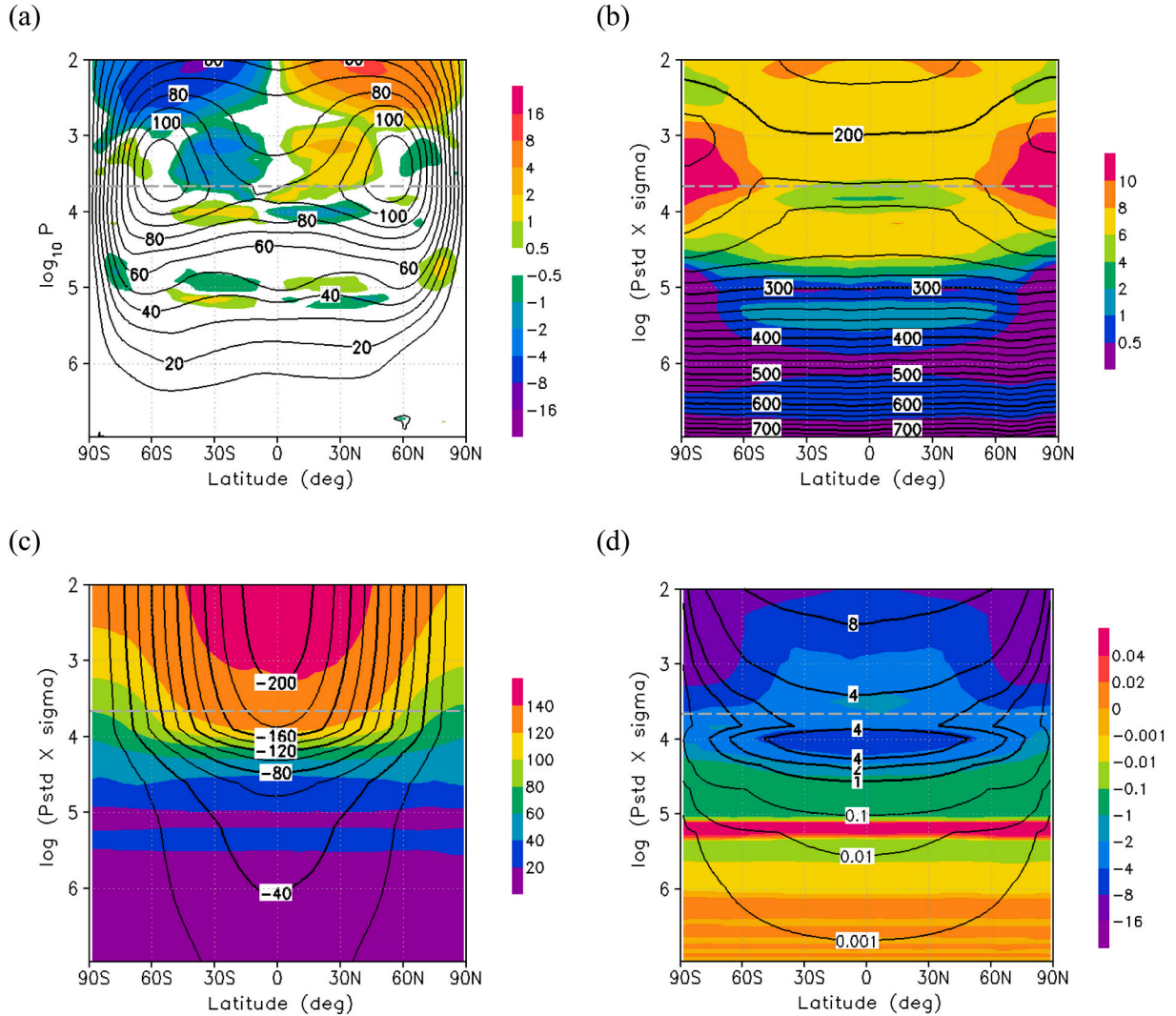


**Fig. 1.** Latitude–pressure distributions of (a) zonal-mean zonal flow ( $\text{m s}^{-1}$ , contours) and meridional flow ( $\text{m s}^{-1}$ , shading), (b) air temperature (K, contours) and static stability ( $\text{K km}^{-1}$ , shading), (c) shortwave (contours) and longwave (shading) radiation fluxes ( $\text{W m}^{-2}$ ), and (d) radiative heating rates ( $\text{K Earth day}^{-1}$ ) due to shortwave (contours) and longwave (shading) radiation, averaged over two Venus days, in the T63 experiments. The gray dash line indicates the altitude of  $4.54 \times 10^3$  Pa ( $\sim 69$  km). (For interpretation of the references to colour in this figure legend, the reader is referred to the web version of this article.)

coordinates, respectively. The zonal mean fields of Eqs. (2) and (3)

$$\overline{X^{TM}} = \overline{X_G^{TM}} = \overline{X_S^{TM}} \quad (4)$$

are investigated in Sections 3.1 and 3.4. Here, the overbar indicates the zonal average over the entire longitudinal range.

In the present work, stationary waves are considered to be topographically locked waves obtained from the data averaged over two Venus days in the geographical coordinates in Section 3.3. The stationary wave is defined as the deviation of the stationary component  $X_G^{TM}$  from the zonal mean:

$$(X_G^{TM})' = X_G^{TM} - \overline{X_G^{TM}}, \quad (5)$$

where the prime is the eddy component. Similarly, thermal tides are solar-locked waves (i.e., stationary waves in the solar-fixed coordinate system), with eddy components described as

$$(X_S^{TM})' = X_S^{TM} - \overline{X_S^{TM}}. \quad (6)$$

in Section 3.2. The diurnal and semidiurnal tides are calculated from zonal wavenumber 1 and 2 components of  $(X_S^{TM})'$ , which are decomposed by fast Fourier transform (FFT).

To investigate the longitudinal variations of the wave activity, we introduce variances of time series data. These statistical quantities are useful for future comparisons with observations because they can be obtained from both model output and satellite measurement. The variances of the meteorological elements in the geographical and solar-fixed coordinates (Section 3.5) are defined as

$$\sigma_G^{TM} = \frac{1}{N} \sum (X_G - X_G^{TM})^2 = \frac{1}{N} \sum X_G^2 - (X_G^{TM})^2, \quad (7)$$

$$\sigma_S^{TM} = \frac{1}{N} \sum (X_S - X_S^{TM})^2 = \frac{1}{N} \sum X_S^2 - (X_S^{TM})^2. \quad (8)$$

In the geographical coordinate system, the variance  $\sigma_G^{TM}$  indicates the activity of unsteady wave components  $(X_G - X_G^{TM})$  excluding the time-mean stationary wave, because the stationary wave component includes the time-mean component  $X_G^{TM}$ . Here the unsteady wave components are composed of planetary-scale migrating waves (e.g., thermal tides and fast Kelvin and Rossby waves) and short-lived, small-scale perturbations (e.g., gravity waves). If the unsteady waves are independent of the surface topography, the variance is zonally uniform. In contrast, if the unsteady wave activity is locally modified by the topography, the variance is highly correlated with the terrain surface. In the solar-fixed coordinates, the variance  $\sigma_S^{TM}$  means the activity of wave components  $(X_S - X_S^{TM})$  excluding the time-mean thermal tides, because the tidal component includes the time-mean component  $X_S^{TM}$ . If the variances strongly depend on local time, the non-tidal wave activity is also modified by solar heating.

In this article, we discuss the longitudinal structures of the time-mean eddy heat and momentum fluxes ( $T_G'v_G'$ ,  $u_G'v_G'$ , and  $u_G'w_G'$  in the geographical coordinates and  $T_S'v_S'$ ,  $u_S'v_S'$ , and  $u_S'w_S'$  in the solar-fixed coordinates) in Section 3.6. If zonally traveling waves independent of the topography rotate around the planet many times, the time-mean fluxes of the wave become the same for all grid points along a given latitude circle (i.e., they are longitudinally uniform). In contrast, the stationary wave pattern is unchanged in the geographical coordinates during the time average period. Thus, the longitudinal variations of the eddy fluxes are produced by stationary waves and their related eddies (e.g., topographically locked convection and gravity waves). In the same way, the local time variations of the eddy fluxes are produced by thermal tides and solar-related gravity waves. For zonally traveling waves independent of the solar heating, the eddy fluxes are longitudinally uniform.

The time and zonal averages of the heat and momentum fluxes of total eddies analyzed in Sections 3.2 and 3.7 are described as

$$(\overline{T'v'})^{TM} = (\overline{T_G'v_G'})^{TM} = (\overline{T_S'v_S'})^{TM}, \quad (9)$$

$$(\overline{u'v'})^{TM} = (\overline{u_G'v_G'})^{TM} = (\overline{u_S'v_S'})^{TM}, \quad (10)$$

$$(\overline{u'w'})^{TM} = (\overline{u_G'w_G'})^{TM} = (\overline{u_S'w_S'})^{TM}. \quad (11)$$

The zonal-mean fluxes of the thermal tides are calculated by

$$(\overline{T'v'})^{tide} = (\overline{T_S^{TM}})'(v_S^{TM})', \quad (12)$$

$$(\overline{u'v'})^{tide} = (\overline{u_S^{TM}})'(v_S^{TM})', \quad (13)$$

$$(\overline{u'w'})^{tide} = (\overline{u_S^{TM}})'(w_S^{TM})'. \quad (14)$$

The zonal-mean fluxes of the stationary wave are

$$(\overline{T'v'})^{stat} = (\overline{T_G^{TM}})'(v_G^{TM})', \quad (15)$$

$$(\overline{u'v'})^{stat} = (\overline{u_G^{TM}})'(v_G^{TM})', \quad (16)$$

$$(\overline{u'w'})^{stat} = (\overline{u_G^{TM}})'(w_G^{TM})'. \quad (17)$$

Zonal-flow acceleration rates of the total eddies, thermal tide, and stationary wave are calculated from the flux convergence of Eqs. (10)–(11), Eqs. (13)–(14) and Eqs. (16)–(17), respectively:

$$F_Y = -1/(rcos^2\varphi) \times \partial(cos^2\varphi \overline{u'v'})^a / \partial\varphi, \quad (18)$$

$$F_Z = -1/\rho \times \partial(\rho \overline{u'w'})^a / \partial z, \quad (19)$$

where  $\rho$  is atmospheric density and the superscript “a” is *TM*, *tide*, or *stat*.

As will be discussed later, the amplitudes and phases of thermal tides are sensitive to altitude around the cloud top. Thus, we investigated the horizontal structures of the eddy heat and momentum fluxes at the two levels: the cloud-heating maximum ( $\sim 65$  km,  $9.75 \times 10^3$  Pa) and cloud top ( $\sim 69$  km,  $4.54 \times 10^3$  Pa) assigned in this article.

### 3. Results

#### 3.1. Overview of the general circulation structure

Fig. 1a and b shows zonally and temporally averaged structures of zonal flow and air temperature. Superrotation is fully developed in the Venus middle atmosphere. Although the zonal jets in the T63 model are  $\sim 10$  m s $^{-1}$  weaker than those in the T21 model (Yamamoto et al., 2019), the zonal-flow and temperature structures are similar in the two models. Our T63 simulation (the present work) reproduces the multi-layered stable layers at low latitudes (Young et al., 1987), the polar strongly stable regions above the  $10^4$ -Pa altitude ( $>65$  km), and the deep low-stability region below the polar stable regions (Tellmann et al., 2009; Ando et al., 2020). These structures are formed by the radiative forcing (Fig. 1c and d), similar to those in the T21 case. Because infrared radiative flux rapidly changes at the cloud bottom ( $\sim 10^5$  Pa,  $\sim 50$  km), the longwave radiation heats the lower part of the low-stability layer and the upper part of the stable region. Thus, the local IR heating produces the layered structure of the static stability around the cloud bottom at low latitudes (e.g., Lee and Richardson, 2011; Lebonnois et al., 2015). Associated with the thermal wind of the zonal jets, polar air temperature is relatively high (low) above (below) the jet core compared to mid-latitude temperature. The polar warming (cooling) enhances high (low) stability around the poles.

The global Hadley circulation is predominant above the cloud top ( $<5 \times 10^3$  Pa,  $>69$  km). In addition, vertically thin Hadley cells form in and around the low-stability layer of  $\sim 10^5$  Pa ( $\sim 50$  km), where the IR heating rate is positive and latitudinally uniform at the cloud base.



Above the cloud top, the equator–pole imbalance between shortwave and longwave radiative fluxes produces strong net radiative forcing (the difference between solar and IR heating), which contributes to the formation of a strong Hadley cell. In contrast, because the radiative heating is locally balanced between shortwave and longwave around the cloud-heating maximum, the net radiative heating of shortwave and longwave becomes weak. Thus, strong poleward flows do not form around  $10^4$  Pa. Indirect circulations are driven around the jet core, where the poleward eddy heat fluxes of thermal tides and baroclinic waves are produced (Yamamoto et al., 2019 and Section 3.7).

### 3.2. Time-mean structure of thermal tides

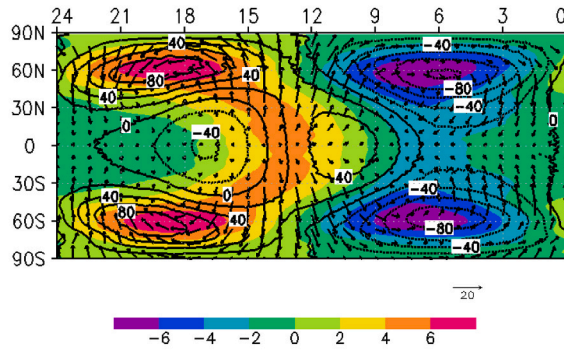
Fig. 2 shows horizontal structures of thermal tides at the cloud top ( $4.54 \times 10^3$  Pa,  $\sim 69$  km) and cloud-heating maximum ( $9.75 \times 10^3$  Pa,  $\sim 65$  km) using Eq. (6). Poleward and eastward flows of the thermal tides are predominant around the subsolar point. At low latitudes, the horizontal flows of the tides have a gravity-wave structure. The thermal tides produce the zonal-wind minimum and strong meridional wind at 12–15 LT, which are consistent with the Akatsuki UVI observations (Yamazaki et al., 2018; Horinouchi et al., 2018) and our T21 simulation (Fig. 9f and Fig. 10 in Yamamoto et al., 2019). The meridional wind magnitude of

the simulated tides is of the same magnitude as in Limaye (1988) and Smith and Gierasch (1996). As discussed in Yamamoto et al. (2019), although the eddy geopotential height and vertical flow are in phase around the equator between  $9.75 \times 10^3$  Pa and  $4.54 \times 10^3$  Pa, the phase of eddy temperature changes rapidly at these pressure levels. At the cloud-heating maximum level of  $9.75 \times 10^3$  Pa, both the eddy temperature and vertical velocity components are positively large around the subsolar point. In contrast, the afternoon temperature is relatively low and the morning and night temperatures are high at low latitudes at  $4.54 \times 10^3$  Pa immediately above the cloud-heating maximum.

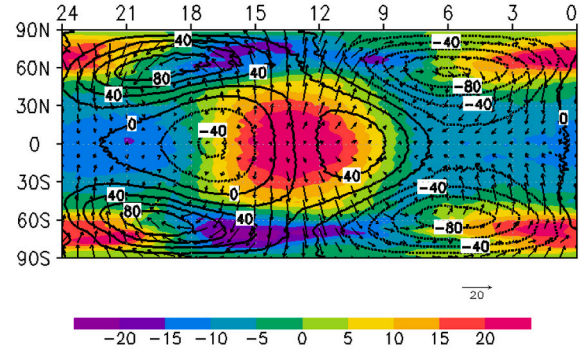
At high latitudes, the horizontal flows of the tides have a vortical structure like a zonal wavenumber-1 Rossby wave (Yamamoto and Takahashi, 2006). The geopotential height and temperature are high (low) around the evening (morning) terminator at  $9.75 \times 10^3$  Pa and  $4.54 \times 10^3$  Pa. Strong meridional flows across the poles are similar to those seen in Yamamoto and Takahashi (2015). Vertical-flow streaks of polar thermal tides are formed along the longitudinally extended trough and ridge at  $\sim 70^\circ$  latitude between the polar low and high.

Both the diurnal and semidiurnal tides are important in our GCM experiments. Fig. 3 shows the horizontal structure of diurnal and semidiurnal tides at the cloud-heating maximum. The diurnal horizontal wind flows from low to high geopotential height at the equator and is a

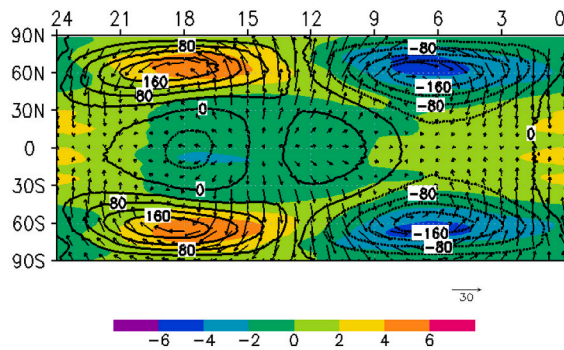
(a)  $9.75 \times 10^3$  Pa ( $\sim 65$  km) ( $T_s^{TM}$ ),



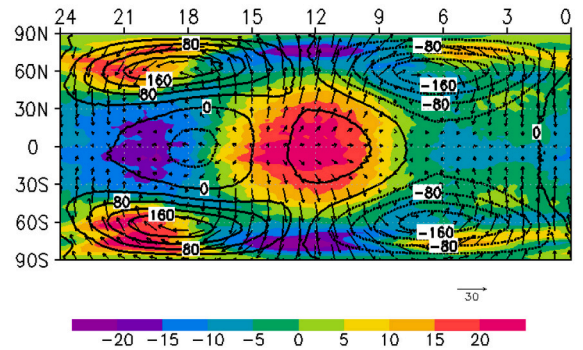
(b)  $9.75 \times 10^3$  Pa ( $\sim 65$  km) ( $w_s^{TM}$ ),



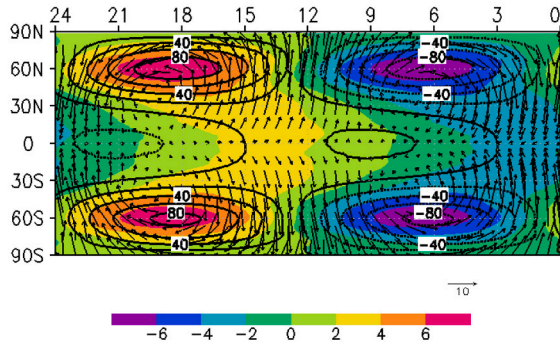
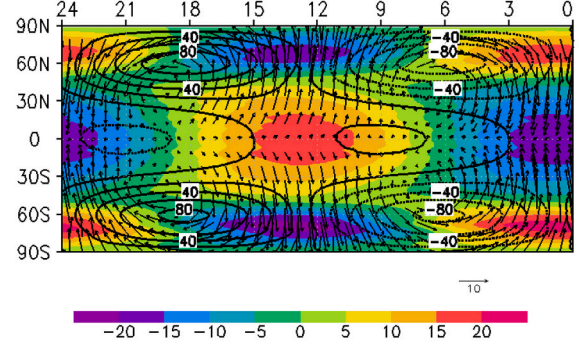
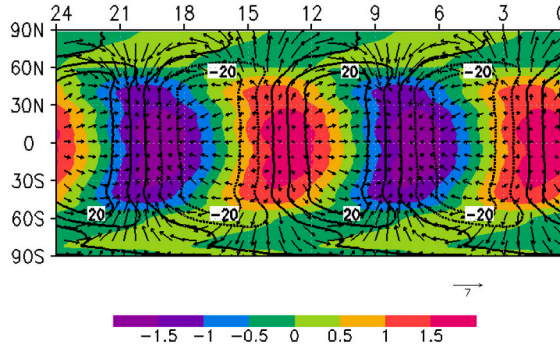
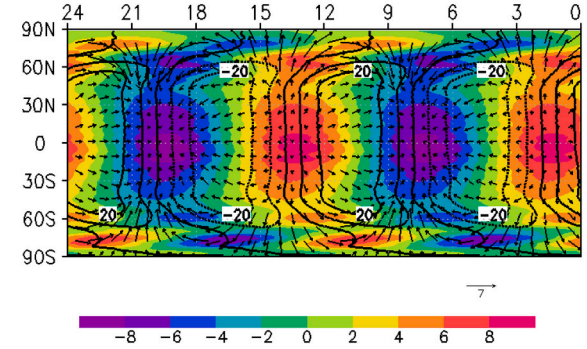
(c)  $4.54 \times 10^3$  Pa ( $\sim 69$  km) ( $T_s^{TM}$ ),



(d)  $4.54 \times 10^3$  Pa ( $\sim 69$  km) ( $w_s^{TM}$ ),



**Fig. 2.** Horizontal distributions of thermal tides obtained from solar-fixed output data averaged over two Venus days. The tidal components of air temperature ( $T_s^{TM}$ )' (K, shading in panels a and c) and vertical wind ( $w_s^{TM}$ )' ( $\text{mm s}^{-1}$ , shading in panels b and d) are shown in solar-fixed coordinates at the levels of (a, b)  $9.75 \times 10^3$  Pa and (c, d)  $4.54 \times 10^3$  Pa, along with the tidal components of zonal wind ( $u_s^{TM}$ )' and meridional wind ( $v_s^{TM}$ )' ( $\text{m s}^{-1}$ , vectors) and geopotential height ( $Z_s^{TM}$ )' (m, contours). Here, the longitude is expressed in terms of local time (LT) and the subsolar point is located at 12 LT. Zonal and meridional winds with positive values indicate westward and northward flow, respectively. (For interpretation of the references to colour in this figure legend, the reader is referred to the web version of this article.)

(a) Diurnal component of  $(T_s^{TM})'$ (b) Diurnal component of  $(w_s^{TM})'$ (c) Semidiurnal component of  $(T_s^{TM})'$ (d) Semidiurnal component of  $(w_s^{TM})'$ 

**Fig. 3.** Horizontal distributions of (a, b) diurnal and (c, d) semidiurnal tides obtained from solar-fixed output data averaged over two Venus days. The tidal components of air temperature  $(T_s^{TM})'$  (K, shading in left panels a and c) and vertical wind  $(w_s^{TM})'$  ( $\text{mm s}^{-1}$ , shading in right panels b and d) at the level of  $9.75 \times 10^3$  Pa ( $\sim 65$  km) are shown in solar-fixed coordinates, along with the tidal components of zonal wind  $(u_s^{TM})'$  and meridional wind  $(v_s^{TM})'$  ( $\text{m s}^{-1}$ , vectors) and geopotential height  $(Z_s^{TM})'$  (m, contours). (For interpretation of the references to colour in this figure legend, the reader is referred to the web version of this article.)

Rossby-like wave at high latitudes. The equatorial maximum of the diurnal temperature component is located around 14 LT, and that of the vertical-wind component is around 13 LT. The diurnal horizontal-flow component diverges poleward from the equatorial temperature maximum. The largest amplitudes of the temperature and vertical flow are located around  $60^\circ$  latitude. The diurnal warm temperature component has a laterally tilted V-shape at low latitudes, where the heat is transported poleward by the horizontal flow. The simulated temperature structure of the diurnal tide is similar to the longwave infrared camera (LIR) observations (Kouyama et al., 2019) at low- and mid-latitudes, although the equatorial maximum is shifted to the afternoon region by a few hours. The maximum amplitude and latitude of the diurnal temperature component are almost the same as those measured by the Pioneer Venus Orbiter Infrared Radiometer Channel 5 ( $\sim 5$  K at  $\sim 60^\circ$  latitude, Pechmann and Ingersoll, 1984), whereas the amplitude is greater than that observed by the Akatsuki LIR ( $\sim 2$  K at  $50^\circ$  latitude).

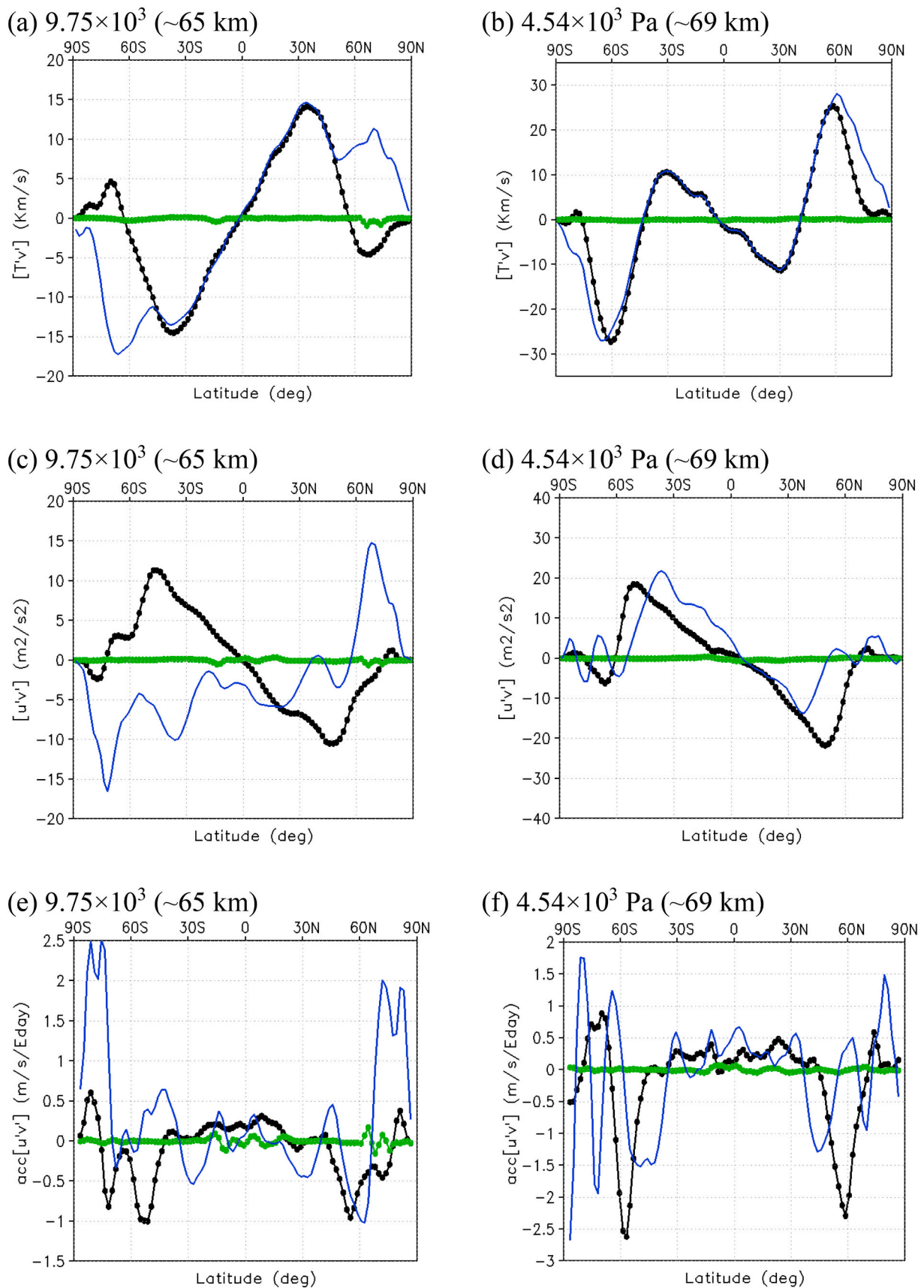
The semidiurnal tides are seen within  $\pm 50^\circ$  latitudes in the GCM. Although the amplitude is almost the same as in the LIR observations, there is a phase shift of 4 LT between our model and the LIR observations (Kouyama et al., 2019).

Fig. 4 shows horizontal meridional momentum and heat fluxes and their convergences. At  $9.75 \times 10^3$  Pa, the thermal tides dominantly transport heat poleward and momentum equatorward at low and mid-latitudes (black line with dots in Fig. 4a and c). Because the strong

meridional flow transports warm air parcels poleward at this level (Fig. 2a), the thermal tides transport heat poleward around the cloud-heating maximum. In the low-latitudinal area within  $\pm 30^\circ$  latitudes, the sign of the eddy heat flux at  $4.54 \times 10^3$  Pa (black line with dots in Fig. 4b) is opposite to that at  $9.75 \times 10^3$  Pa (black line with dots in Fig. 4a) because the phases of the air temperature component change at these two pressure levels (Fig. 2a and c). The meridional profiles of eddy momentum fluxes at  $4.54 \times 10^3$  Pa (black line with dots in Fig. 4d) are similar to those at  $9.75 \times 10^3$  Pa (black line with dots in Fig. 4c). Because the strong horizontal wind vectors tilt eastward with increasing latitude in the regions of 9–12 LT and 18–21 LT in Fig. 2, they transport the zonal momentum equatorward at  $9.75 \times 10^3$  Pa and  $4.54 \times 10^3$  Pa. The horizontal heat and momentum fluxes of the thermal tides (black line with dots) are symmetrical across the equator because of the symmetrical thermal forcing, while those of the stationary waves (green line with dots) are trivial around the cloud top. The transient eddies excluding thermal tide and stationary wave might produce the latitudinally asymmetrical structure of the heat and momentum fluxes, because the topography produces the latitudinal asymmetry of the bottom boundary and the basic (zonal-mean) field of the transient eddies. Thus, the asymmetry of the heat and momentum transport is produced by total eddies (blue lines).

The equatorward momentum fluxes produce zonal-flow accelerations of  $0.2\text{--}0.5 \text{ m s}^{-1}$  Earth day $^{-1}$  at low latitudes in Fig. 4e and f. This is





**Fig. 4.** Latitudinal distributions of zonal-mean (a, b) meridional heat fluxes, (c, d) meridional momentum fluxes, and (e, f) zonal flow acceleration due to the horizontal momentum flux at  $9.75 \times 10^3$  Pa (left column) and  $4.54 \times 10^3$  Pa (right column). The quantities are averaged over two Venus days. The blue line, black line with dots, and green line with dots are the meridional fluxes associated with total eddies, thermal tides, and steady stationary waves, respectively. (For interpretation of the references to colour in this figure legend, the reader is referred to the web version of this article.)

of the same magnitude as the acceleration around the cloud-heating maximum via the vertical propagation of thermal tides (see later Fig. 7c). The polar zonal-flow acceleration by thermal tides (black line with dots in Fig. 4e) is one-fifth weaker than that by total waves (blue line in Fig. 4e) on the poleward flank of the high-latitude jet at  $9.75 \times 10^3$  Pa. At  $4.54 \times 10^3$  Pa (black line with dots in Fig. 4f), the weak zonal-flow acceleration by tides is formed within  $\pm 30^\circ$  latitudes, whereas the deceleration is locally strong around the jet cores ( $60^\circ$  latitudes). This is quite different from the complex profile of acceleration by total waves. In particular, because the small-scale meridional variation of the momentum fluxes of total waves is large at high latitudes, the acceleration profile of total waves at high latitudes is more complex than that at low latitudes.

Fig. 5 shows local-time-pressure distributions of air temperature of thermal tides along with solar-locked static stability. Here the local-time variation of the static stability is primarily produced by the thermal tides because the non-tidal eddy components are efficiently removed by the long-term average over two Venus days. At the equator, the tidal structure is almost the same as in the T21 experiment. Thermal tides propagate upward above (downward below) the cloud top (gray dashed line,  $\sim 69$  km). In and above the equatorial cloud layer of  $> 50$  km ( $\sim 10^5$  Pa), the large temperature amplitudes of  $> 4$  K produce the longitudinal variation of the static stability. The amplitudes are consistent with those in radio-occultation observations and a simplified model using Newtonian cooling (Ando et al., 2018). The local minimum of static stability is located in the afternoon area (12–18 LT) around the cloud-heating maximum ( $\sim 65$  km,  $10^4$  Pa) due to the solar radiation. A locally high static stability around 80 km ( $\sim 5 \times 10^2$  Pa) at 17 LT in Ando et al. (2018) is seen around  $10^2$  Pa and 21 LT in our model (Fig. 5a).

The midlatitude thermal tide has a negative (positive) temperature deviation at 0–12 LT (12–24 LT) at  $\sim 10^4$  Pa and  $51.3^\circ$  S latitude and propagates vertically. The negative temperature signal extends from  $10^4$  Pa at 0–12 LT to  $10^3$  Pa ( $\sim 75$  km) at 10–16 LT. This is similar to results from the GCM of the Institut Pierre Simon Laplace (IPSL) and the Visible and Infrared Thermal Imaging Spectrometer (VIRTIS) in the night at  $45^\circ$  S latitude (Scarica et al., 2019), though the strong negative signal at 0–6 LT in our model is not seen in the observations between  $10^3$  and  $10^2$  Pa (75 and 85 km).

At  $69.9^\circ$  N latitude, the zonally uniform structure of the static stability is predominant because the vertical gradient of zonal-mean temperature is relatively larger than that of eddy temperature. Around the cloud-heating maximum ( $9.75 \times 10^3$  Pa,  $\sim 65$  km), positive and negative temperature deviations are located at 12–24 LT and 0–12 LT, respectively. This is consistent with those in the IPSL GCM and VIRTIS at high latitudes (Scarica et al., 2019). The thermal tide propagates upward above the  $10^4$ -Pa altitude ( $> 65$  km). The temperature amplitude of the upward propagating tide is weaker than that at the equator around  $10^3$  Pa because of weaker solar insolation at higher latitudes. The thermal tide propagates downward below the  $10^5$ -Pa altitude ( $\sim 50$  km).

Fig. 6 shows vertical structures of the air temperature components of diurnal and semidiurnal tides. The vertical tilt of the diurnal tide phase is steeper than that of the semidiurnal tide at the equator above the altitude of the  $10^5$  Pa level ( $\sim 50$  km). Such a difference in the phase between diurnal and semidiurnal tides is also seen in Pechmann and Ingersoll (1984). The eddy temperatures are amplified around  $10^4$  Pa ( $\sim 65$  km) and  $5 \times 10^4$  Pa ( $\sim 56$  km) in Fig. 6a and b. The diurnal tide propagates from the cloud-heating maximum to the near-surface (Fig. 6a). The semidiurnal tide forced at the cloud-heating maximum reaches the  $10^5$ -Pa level (Fig. 6b). Below this level, the semidiurnal temperature component is amplified in the weakly stable layer at  $\sim 2 \times 10^5$  Pa ( $\sim 45$  km) and propagates downward to the near-surface. According to the simplified GCM of Takagi et al. (2018), the diurnal and semidiurnal thermal tides dissipate abruptly around 80 km height, where the Doppler-shift velocity of the thermal tides is low ( $|\bar{u} - c| < 10$  m s $^{-1}$ ). In Sugimoto et al. (2017), the distributions of the zonal mean winds above the cloud top are quite different from those in our work and

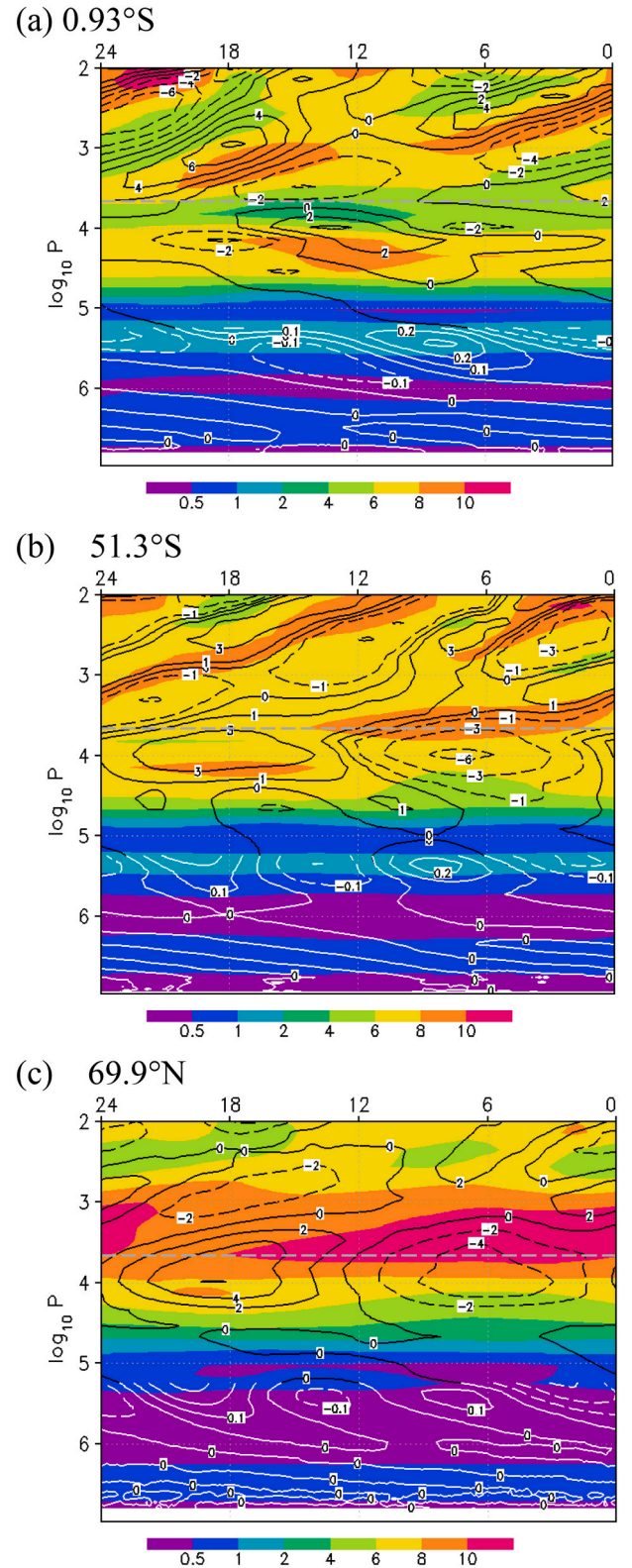
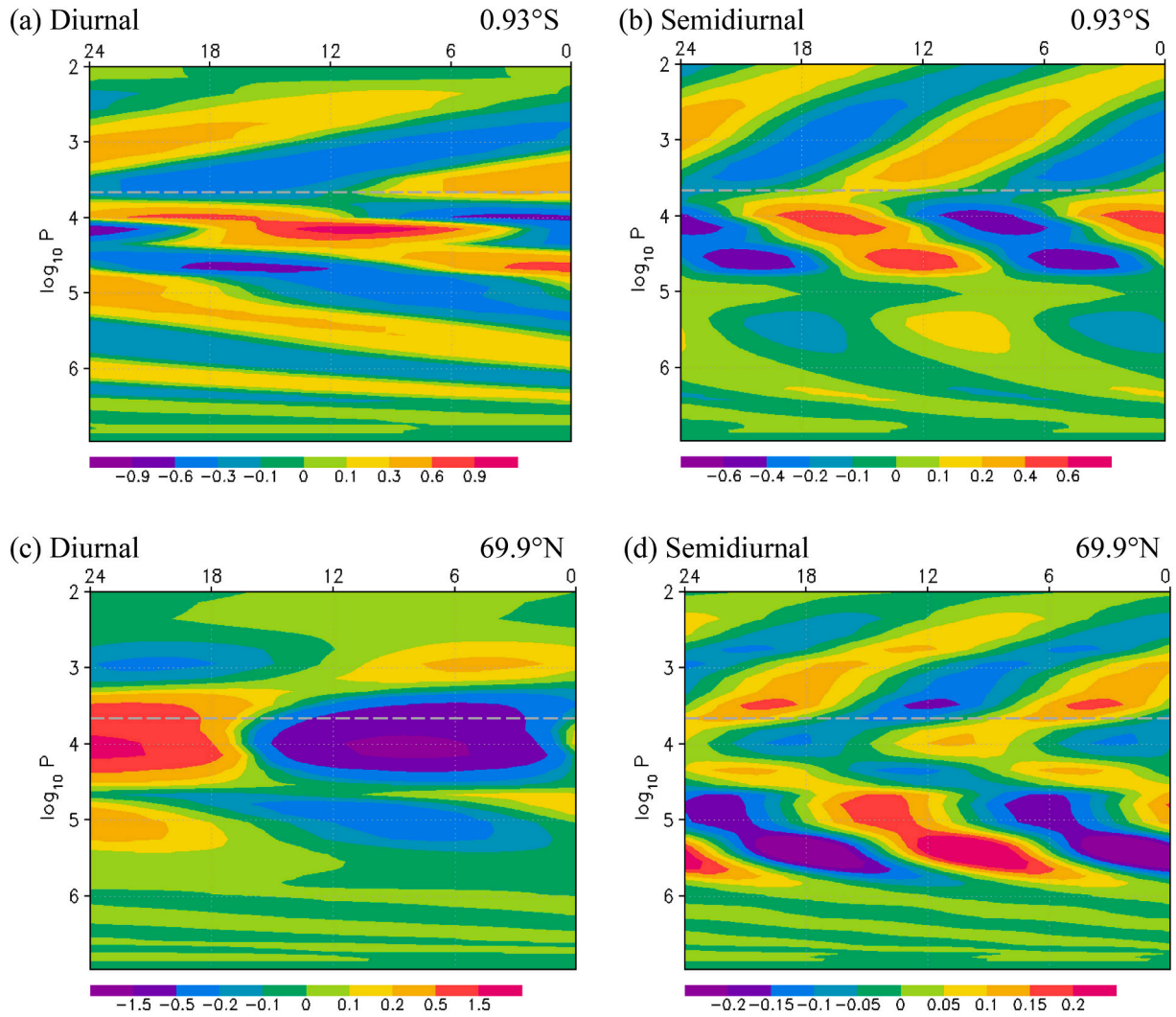


Fig. 5. Local-time-pressure distributions of thermal tide components of air temperature ( $T_s^{TM}$ ) (K, contour), along with static stability ( $K\ km^{-1}$ , shading) at (a)  $0.93^\circ$  S, (b)  $51.3^\circ$  S and (c)  $69.9^\circ$  N latitude. The white contours with a small interval of 0.05 K are shown below the altitude of  $1.58 \times 10^5$  Pa. Gray dash line indicates the altitude of  $4.54 \times 10^3$  Pa ( $\sim 69$  km). (For interpretation of the references to colour in this figure legend, the reader is referred to the web version of this article.)





**Fig. 6.** Local-time–pressure distributions of (a, c) diurnal and (b, d) semidiurnal tide components of air temperature ( $T_s^{\text{TM}}$ )' (K) at (a, b) 0.93°S and (c, d) 69.9°N latitude. Shaded values are weighted by the square root of  $P(\text{Pa})/101,325(\text{Pa})$ . The gray dash line indicates the altitude of  $4.54 \times 10^3$  Pa (~69 km). (For interpretation of the references to colour in this figure legend, the reader is referred to the web version of this article.)

the amplification of the eddy temperature by solar heating above 80 km was not reported. Thus, the vertical and horizontal structures of thermal tides in their works are different from those in our work. In our T63 GCM experiment, the sub-solar solar heating rate is  $\sim 20 \text{ K day}^{-1}$  and the zonal-mean equatorial infrared cooling rate is  $\sim 5 \text{ K day}^{-1}$  around  $3.62 \times 10^2$  Pa (~81 km, where the Doppler-shift velocities are high ( $\sim 60 \text{ m s}^{-1}$ )). Therefore, the thermal tides forced by strong solar heating and dissipated by infrared cooling propagate vertically in the upper atmosphere in our work. To elucidate the difference with the observations and previous GCMs, the sensitivity of thermal tides to the zonal-mean field (i.e., the basic field of the waves) and solar heating must be also further investigated.

At high latitudes where tidal vertical momentum flux is high (see later Fig. 17b), the diurnal tide is amplified and the vertical propagation is not apparent around  $10^4$  Pa (Fig. 6c). The semidiurnal tide is forced at the cloud-heating maximum ( $\sim 10^4$  Pa) and propagates upward and downward there (Fig. 6d). It is enhanced or re-forced in the region between  $10^5$  Pa (~50 km) and  $10^6$  Pa (~30 km) where the static stability is low in Fig. 5c.

Fig. 7 shows vertical momentum fluxes of thermal tides and their convergences (black line with dots). The thermal wave is a primary transporter of the vertical momentum at and above the cloud-heating maximum ( $\sim 10^4$  Pa) in Fig. 7a. At the equator, the vertical

momentum flux of thermal tides has two negative maxima at  $\sim 7 \times 10^3$  Pa (~67 km) and  $\sim 6 \times 10^2$  Pa (~79 km) and two positive maxima at  $\sim 3 \times 10^4$  Pa (~58 km) and  $\sim 5 \times 10^5$  Pa (~36 km) (black line with dots in Fig. 7a). This suggests that radiative heating primarily forces the thermal tides around the cloud-heating maximum ( $\sim 10^4$  Pa in Fig. 1d) and weakly amplifies their vertical momentum flux at  $6 \times 10^2$  Pa and  $\sim 5 \times 10^5$  Pa. The equatorial zonal-flow accelerations of  $\sim 0.5 \text{ m s}^{-1} \text{ Earth day}^{-1}$  are located at  $1 \times 10^4$  Pa and  $9 \times 10^2$  Pa (~77 km). The deceleration of  $\sim 0.5 \text{ m s}^{-1} \text{ Earth day}^{-1}$  is located at  $3 \times 10^3$  Pa (~71 km) in Fig. 7c (black line with dots).

The vertical profile of the vertical momentum flux of the tides at high latitudes is different from that at the equator: there are a negative maximum around  $1 \times 10^4$  Pa (~65 km) and two positive maxima at  $2.8 \times 10^5$  Pa (~42 km) and  $3.1 \times 10^3$  Pa (~71 km) in Fig. 7b (black line with dots). The high-latitude tides accelerate zonal flow at a rate of  $\sim 3 \text{ m s}^{-1} \text{ Earth day}^{-1}$  around  $1.4 \times 10^3$  Pa (~85 km) and  $1.4 \times 10^2$  Pa (~75 km) and decelerate it at a rate of  $\sim 1 \text{ m s}^{-1} \text{ Earth day}^{-1}$  around  $6.7 \times 10^3$  Pa (~67 km) and at a rate of  $\sim 3 \text{ m s}^{-1} \text{ Earth day}^{-1}$  around  $3.6 \times 10^2$  Pa (~81 km) (black line with dots in Fig. 7d). The level of the strong zonal-flow acceleration at high latitudes is located above the cloud top. The zonal-flow acceleration rate is six-times greater than at the equator.

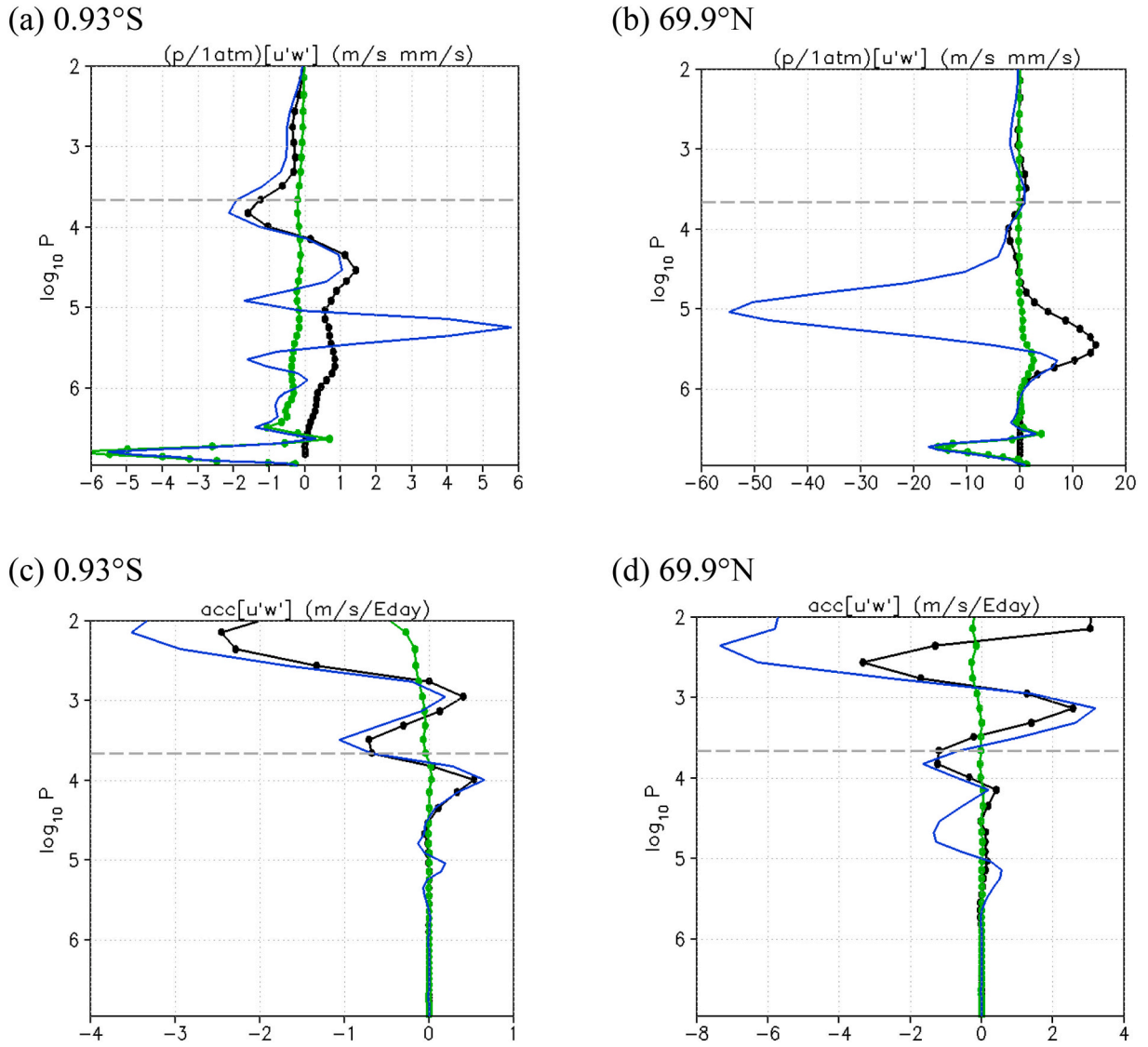


**Fig. 7.** Vertical distributions of zonal-mean (a, b) pressure-weighted vertical momentum fluxes and (c, d) zonal flow acceleration due to the vertical momentum flux at (a, c) 0.93°S and (b, d) 69.9°N latitude. The quantities are averaged over two Venus days. The blue line, black line with dots, and green line with dots are the fluxes associated with total eddies, thermal tides, and steady stationary waves, respectively. The gray dash line indicates the altitude of  $4.54 \times 10^3$  Pa ( $\sim 69$  km). (For interpretation of the references to colour in this figure legend, the reader is referred to the web version of this article.)

### 3.3. Time-mean structures of stationary waves

Fig. 8 shows temporally averaged stationary structures of meteorological elements at the cloud top using Eq. (5). Differently from the T21 experiments, small-scale stationary waves are predominant in the T63 experiment at low latitudes, together with laterally tilted global V shapes. For eddy vertical flow, topographically-locked bow shapes are locally enhanced over the equatorial highlands. Although the topographically-locked bow shapes are reminiscent of the bow-shaped streaks, they are not the same as the brightness temperature image of a huge bow-shaped wave observed by the Akatsuki LIR (Fukuhara et al., 2017), which depends on the local time (Kouyama et al., 2017). Latitudinally large-scale streaks of eddy temperature and meridional flow extend from the Aphrodite Terra to high latitudes. Close to the poles, the stationary patches of temperature and meridional flow have zonal wavenumber 2 to 4. In addition, the fine-scale streaks (high zonal wavenumber component) of these meteorological elements are also seen in the high-resolution model, though they are not seen in the low-resolution model (Yamamoto et al., 2019). Because these stationary wave amplitudes are much smaller than those of the thermal tides, the

horizontal heat flux of the stationary waves is very small (green curve with dots in Fig. 4a), although the phases of the eddy components are horizontally tilted in the horizontal structure of the temperature and meridional flow. In our model, the bow-shaped temperature pattern is not apparent, different from the LIR. According to Lefèvre et al. (2020), smaller-scale temperature patterns are amplified over the high mountains in a mesoscale non-hydrostatic simulation of topographically-forced waves. They are not simulated in our hydrostatic T63 GCM. Thus, we might need to further investigate the topographical and local-time dependence of the stationary, huge bow-shaped gravity waves in the LIR images using high-resolution non-hydrostatic simulations.

As abovementioned, the wave pattern of vertical flow is quite different from those of air temperature and horizontal flow. Both planetary-scale and small-scale wave components are seen for the temperature (Fig. 8a) and horizontal flow (Fig. 8b and d), whereas only fine-scale eddies (bow-shaped streaks with high zonal wavenumber) are predominant for the vertical flow (Fig. 8c). Compared to the horizontal-wind magnitude  $U$ , the vertical-wind magnitude  $W$  is very small for the large horizontal scale  $L$  and small vertical scale  $H$  (scale height) according to the scale analysis of the continuity equation (e.g., Holton,

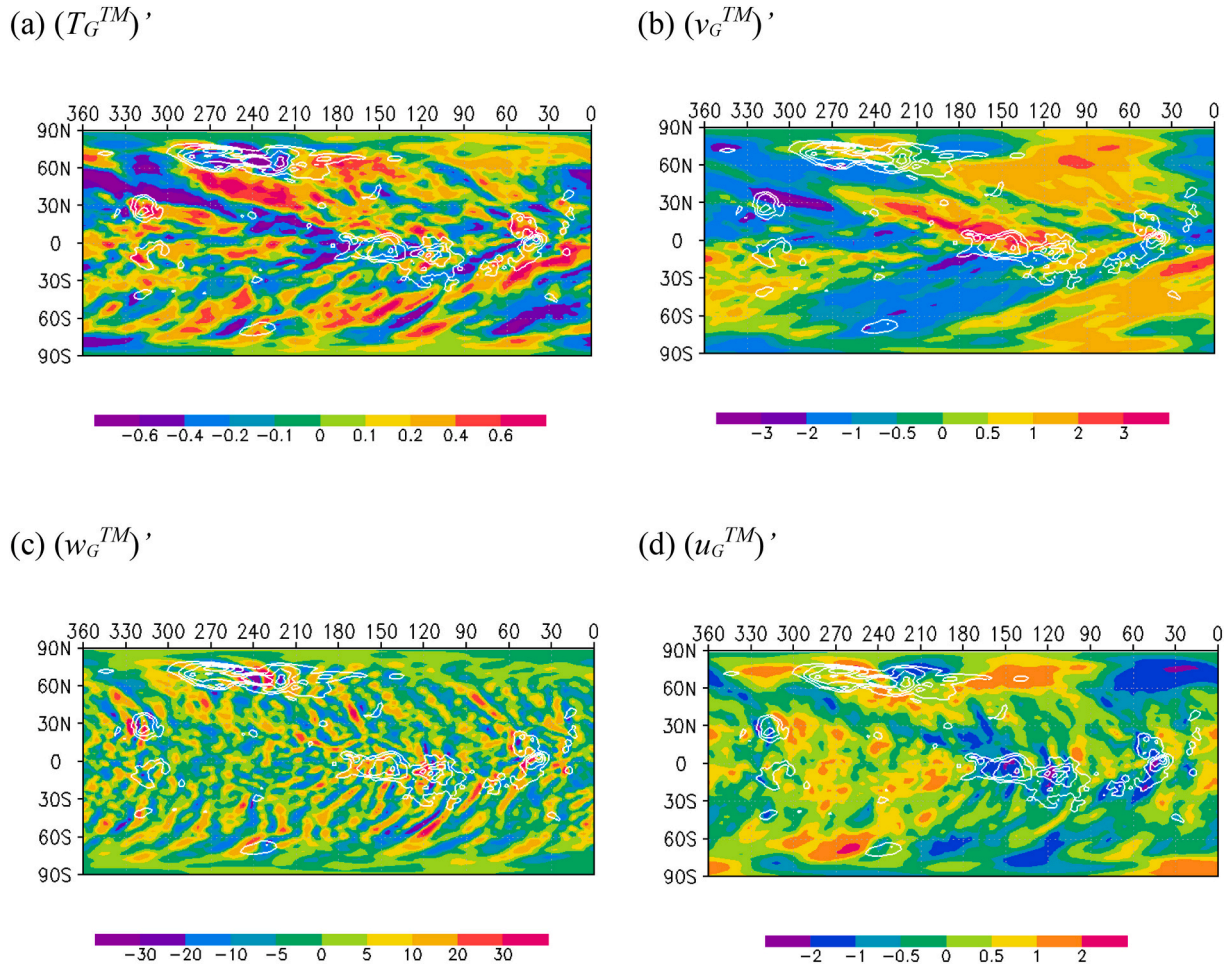


**Fig. 8.** Geographical longitude-latitude distributions of steady stationary waves obtained from topographically locked output data averaged over two Venus days. The eddy components of (a) air temperature ( $T_G^{TM}$ )' (K), (b) meridional wind ( $v_G^{TM}$ )' ( $\text{m s}^{-1}$ ), (c) vertical wind ( $w_G^{TM}$ )' ( $\text{mm s}^{-1}$ ) and (d) zonal wind ( $u_G^{TM}$ )' ( $\text{m s}^{-1}$ ) at the cloud-top level of  $4.54 \times 10^3$  Pa ( $\sim 69$  km) are shown in geographical coordinates. White contours (695, 705, and 715 K) indicate the lowermost-level temperature change that is modified by surface topography. (For interpretation of the references to colour in this figure legend, the reader is referred to the web version of this article.)

2004):  $W \sim H/L \times U$ . Thus, for the vertical flow, it is difficult to see the weak planetary-scale component, while the fine-scale bow-shaped waves are more apparent.

Within the fine-scale bow-shapes of strong eddy vertical wind, the magnitudes of these vertical winds are enhanced around the low-latitude highlands and extend from these low-latitude areas toward the poles. Such active vertical motion over the highlands supports the work of Peralta et al. (2017), who reported that stationary wave patterns were concentrated over regions of higher surface elevation. The eddy zonal wind locally slows over the Aphrodite Terra. However, the negative deviation of eddy zonal wind ( $\sim 2 \text{ m s}^{-1}$ ) is 10% of the local wind slowness ( $\sim 20 \text{ m s}^{-1}$ ) detected by Bertaux et al. (2016).

The vertical structures of the stationary waves at the equator are quite different from those at a high latitude in Fig. 9. At the equator (Fig. 9a, c, and e), high zonal wavenumbers are predominant and the phase lines are not tilted but are almost vertical. The eddy vertical wind is enhanced over the high mountains. Small-scale patches of the eddy zonal flow and temperature are predominant in the cloud layer and may be driven by stationary wave breaking. The stationary gravity waves are predominant above the cloud top (gray dashed line), where static stability is high. The negative phase of the eddy zonal flow gives a local wind decrease at the cloud top over the Aphrodite Terra. However, there are regions of increased local wind immediately below 69 km. Thus, the observation of local wind decrease over the Aphrodite Terra (Bertaux

et al., 2016) may be sensitive to the height of the UV detection.

At high latitudes, planetary-scale stationary waves propagate vertically above the cloud top (gray dashed line in Fig. 8b and d). In the lower atmosphere, the standing phase structures are localized over the Maxwell Montes (Fig. 9b, d, and f). In addition, vertical tilting of the stationary eddy zonal flow is just about visible below the  $10^4$ -Pa altitude ( $< 65$  km, Fig. 9b). The standing wave or convection localized over the Maxwell Montes penetrates into the cloud layer and might forces or enhances the vertical propagating waves around  $10^4$  Pa. The downward wave propagation from  $\sim 10^4$  Pa toward the surface produces positive vertical momentum flux between  $10^6$  and  $10^5$  Pa (30 and 50 km) around  $70^\circ\text{N}$  latitude (see later in the right panel of Fig. 17c).

### 3.4. Topographical impacts on the general circulation

To evaluate the topographical effects on the general circulation, we discuss the difference in the zonal-mean flow between the experiments with and without topography in Fig. 10. In the T63 flat experiment (Flat), the strong zonal flow and Hadley cells are also seen in and above the cloud top and the vertically thin cells are around  $10^5$  Pa ( $\sim 50$  km). However, the general circulation is not the same as in the experiment with the surface topography (Topo). In the T63 experiments, the reduction in zonal-flow speed caused by the topography is predominant above the  $10^3$ -Pa altitude, in the equatorial region between  $10^6$  Pa ( $\sim 30$



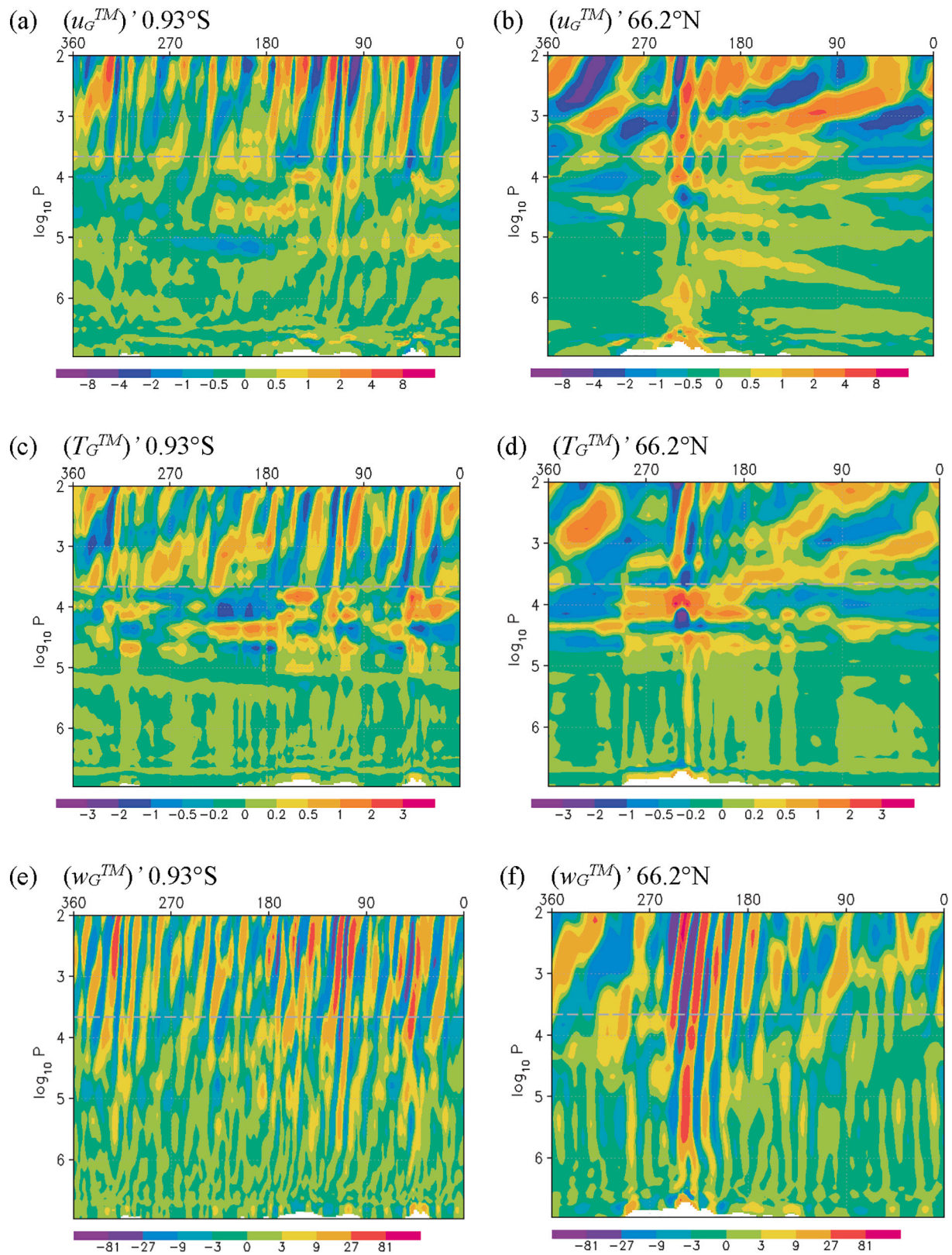


**Fig. 9.** Geographical longitude-pressure distributions of steady stationary eddy components of (a, b) zonal wind ( $u_G^{TM}$ )' ( $\text{m s}^{-1}$ ), (c, d) air temperature ( $T_G^{TM}$ )' (K), and (e, f) vertical wind ( $w_G^{TM}$ )' ( $\text{mm s}^{-1}$ ), averaged over two Venus days at (a, c, e)  $0.93^\circ\text{S}$  and (b, d, f)  $66.2^\circ\text{N}$  latitude. The gray dash line indicates the altitude of  $4.54 \times 10^3 \text{ Pa}$  ( $\sim 69 \text{ km}$ ). (For interpretation of the references to colour in this figure legend, the reader is referred to the web version of this article.)

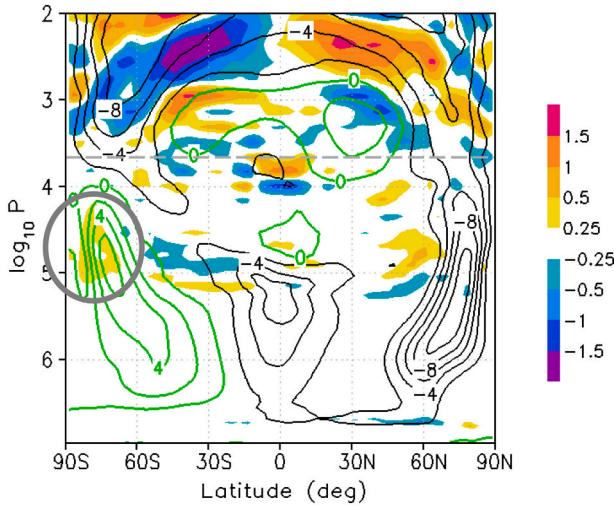


**Fig. 10.** Latitude–pressure distributions of the differences in zonal (contour) and meridional (shading) flows ( $\text{m s}^{-1}$ ) between the experiments with and without topography (termed Topo and Flat, respectively), averaged over two Venus days. Green contours mean that the zonal flow in Topo is faster than in Flat. The gray dash line indicates the altitude of  $4.54 \times 10^3$  Pa ( $\sim 69$  km). (For interpretation of the references to colour in this figure legend, the reader is referred to the web version of this article.)

km) and  $10^5$  Pa ( $\sim 50$  km), and below the  $10^4$ -Pa altitude ( $\sim 65$  km) over the Maxwell Montes ( $50$ – $80^\circ\text{N}$ ). In contrast, the topography enhances zonal flow in the low-latitudinal region between  $10^4$  Pa ( $\sim 65$  km) and  $10^3$  Pa ( $\sim 75$  km) and in the southern high-latitudinal region below the  $10^4$ -Pa altitude. The zonal-flow increase caused by the topography in the T63 simulation above the cloud top supports the results of Lebonnois et al. (2010), who reported that the zonal flow in the presence of topography is faster than that under the flat-surface condition around 70 km. Such a topographical enhancement of the superrotational flow is not seen in the T21 experiments of Yamamoto and Takahashi (2009) and Yamamoto et al. (2019). The topography in our T63 experiment intensifies the poleward flow ( $\bar{v}$ ) of the Hadley cell above the  $10^3$ -Pa altitude ( $>75$  km) and vertically-thin Hadley circulation around  $10^5$  Pa. The meridional-flow difference is positive (i.e., the poleward flow is weakened) in the upper portion of the region where the topography enhances the zonal flow (gray circle in Fig. 10).

Fig. 11 shows latitude–pressure distributions of the metric-term ( $\bar{u} \bar{v} \tan \varphi / r$ ) and the convergence of eddy vertical momentum flux ( $-\rho^{-1} \partial(\rho \bar{u} \bar{w}) / \partial z$ ), along with the differences between the Topo and Flat experiments. The acceleration/deceleration due to the metric term corresponds to the zonal-mean poleward/equatorward flow (Fig. 1a). The eddy vertical momentum flux decelerates the zonal flows above the  $10^3$ -Pa altitude ( $>75$  km), whereas the zonal-flow acceleration areas are also seen around the cloud-heating maximum (within  $\pm 30^\circ$  latitudes,  $\sim 10^4$  Pa,  $\sim 65$  km) and on the polar flank of the jet (Fig. 11b). At low latitudes, the zonal-flow acceleration by eddy vertical momentum flux is somewhat intensified around the cloud top (positive difference, yellow shading in Fig. 11d) and the deceleration is also intensified above the  $10^3$ -Pa altitude (positive difference, blue shading in Fig. 11d) in the Topo experiment. This indicates that the topography leads to the enhancement of the equatorial zonal-flow around the cloud top and its vertical shear above the cloud top.

At high latitudes where  $|\varphi| \geq 60^\circ$ , the deceleration by eddy vertical momentum flux approximately balances the metric-term acceleration above the  $10^3$ -Pa altitude ( $>75$  km) and between  $10^5$  Pa ( $\sim 50$  km) and  $10^4$  Pa ( $\sim 65$  km). The momentum balance indicates that the zonal-flow deceleration caused by eddies maintains the product of the poleward and super-rotational flows via the metric term ( $\bar{u} \bar{v} \tan \varphi / r$ ), different from the Earth's middle atmosphere in which the Coriolis force  $2\Omega \bar{v} \sin \varphi$

enhances only a poleward flow in the downward control principle (Haynes et al., 1991; Imamura, 1997). In high-latitudinal regions between  $10^5$  Pa and  $10^4$  Pa at high latitudes, the metric-term acceleration (negative difference, blue shading in Fig. 11c) and the zonal-flow deceleration by eddies (positive difference, orange shading in Fig. 11d) weaken in the presence of the topography. Compared to the Flat experiment, the decrease in the zonal flow  $\bar{u}$  reduces the metric term ( $\bar{u} \bar{v} \tan \varphi / r$ ) (black contours and blue shading in the gray dotted circle of Fig. 11c) in the Topo experiment, while there is no large difference in the meridional flow between the Topo and Flat experiments. In contrast, the zonal flow is increased (green contours in the gray solid circle of Fig. 11d) by the decrease in the deceleration by  $-\rho^{-1} \partial(\rho \bar{u} \bar{w}) / \partial z$  (orange shading in the gray solid circle of Fig. 11d) in the southern polar region between  $10^5$  Pa and  $10^4$  Pa where there are not high mountains. In this case, the decrease in the poleward flow  $\bar{v}$  (gray circle in Fig. 10) reduces the metric term of  $\bar{u} \bar{v} \tan \varphi / r$  (blue shading in the gray circle of Fig. 11). Thus, in the momentum balance between the convergence of eddy vertical momentum flux and metric term, the decrease in the metric term due to the topography produces the decrease/increase in the zonal flow in the northern/southern polar regions, which leads to the asymmetry of the zonal flow between the southern and northern polar regions.

### 3.5. Longitudinal and local-time structures of variances

The variance  $\sigma_G^{TM}$  of the time series data in geographical coordinates indicates the activity of unsteady waves, which excludes the time-mean stationary waves, as noted in Section 2.2. If the variance is zonally uniform, the unsteady wave activity is independent of the surface topography and stationary waves. In contrast, if the longitudinal variation of the variance is highly correlated with the surface terrain in geographical coordinates, it is produced by the topography. In Fig. 12, the variances are very small below the  $10^5$ -Pa altitude ( $<50$  km) and amplified at multi-levels above this altitude. Thus, the unsteady eddy activity locked to the topography is not only directly forced by the surface but also modified by stationary waves in and above the cloud layer (above the  $10^5$ -Pa altitude). For the variance of vertical flow (Fig. 12a), vertical spikes are apparent slightly west of the summits of the equatorial mountains (the white region around the bottom of the figure). These spikes of the vertical flow are suggestive of penetrative plumes and vertically propagating gravity waves. In the infrared heating region at  $\sim 10^5$  Pa, the variance of the vertical flow is regionally high over the equatorial lowlands. Vega balloons had shown active vertical motion around the cloud bottom (Ingersoll et al., 1987). Although the convective motion or gravity waves detected by the balloon experiments are not fully resolved in GCMs, the high variances of vertical and zonal flows around  $10^5$  Pa in our model indicate the large-scale ( $\sim 1000$  km) convective motion. In the convectively active layer ( $\sim 10^5$  Pa), where the static stability is low, the variance of air temperature is low (Fig. 12c). A thin layer of the high variance of air temperature is located around the cloud-heating maximum (orange shading around  $10^4$  Pa in Fig. 12c). The temperature variance in the thin layer is regionally low over the equatorial high lands.

At  $66.2^\circ\text{N}$  latitude, the variances of vertical and horizontal flows are high above the  $10^4$ -Pa altitude ( $>65$  km) in Fig. 12d and e. A layer of the weakly high variance of vertical flow is also seen around  $10^5$  Pa ( $\sim 50$  km). The variance of air temperature is high around the  $10^4$ -Pa altitude and above the  $10^3$ -Pa altitude ( $>75$  km), whereas it is low around  $2.1 \times 10^3$  Pa ( $\sim 73$  km). This implies that the eddy temperature of unsteady waves is weakened in the polar stable region between  $10^4$  Pa and  $10^3$  Pa, where the static stability is extremely high ( $>10$  K/m). Unsteady eddies excluding the stationary waves are locally generated or enhanced over the Maxwell Montes. The vertical spike of vertical flow is barely visible around  $240^\circ$  longitude in Fig. 12d. The variance of air temperature at  $\sim 10^4$  Pa is regionally high between  $200^\circ$  and  $270^\circ$  longitudes in Fig. 12f,



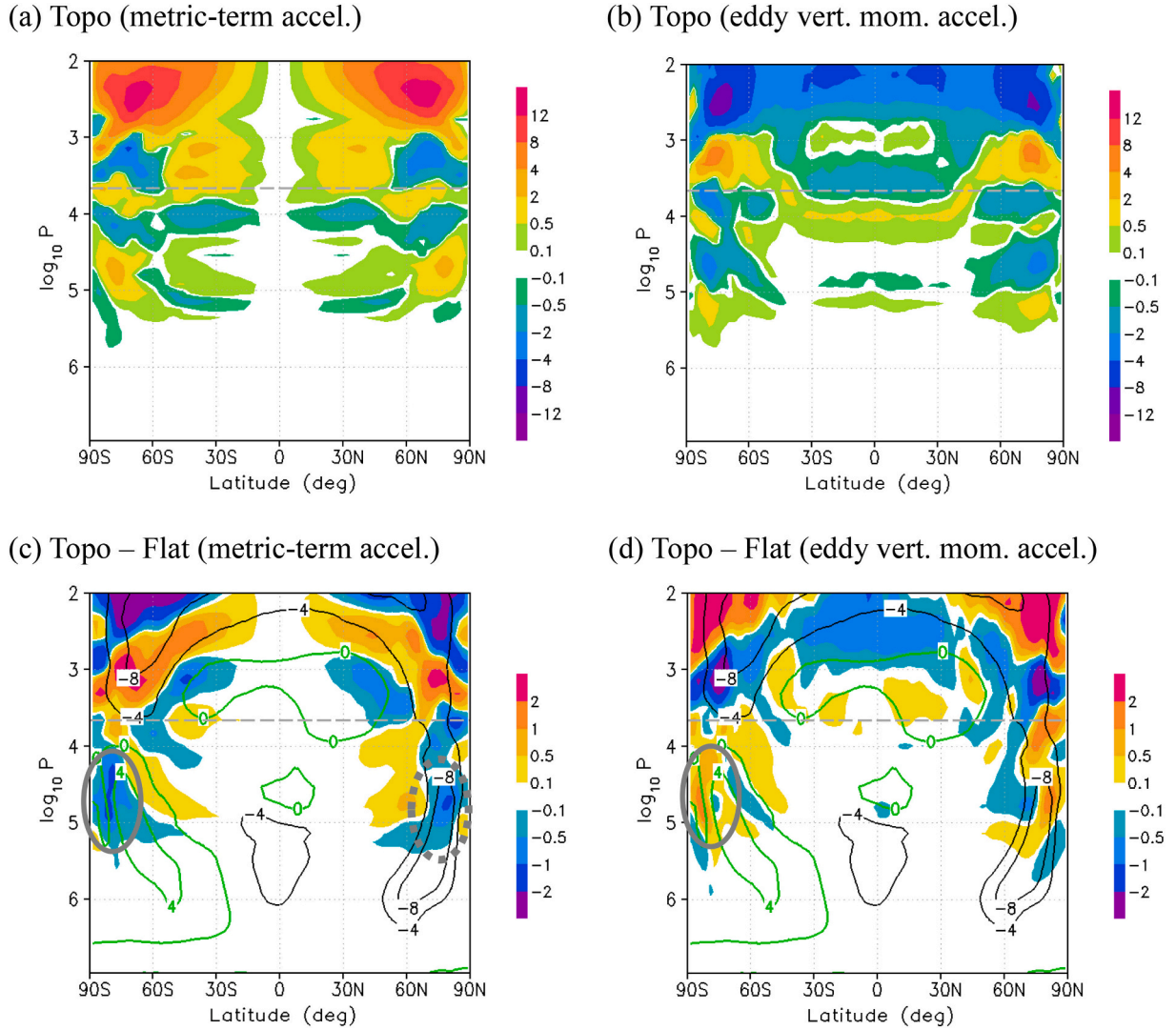


**Fig. 11.** Latitude–pressure distributions of (a) metric-term acceleration ( $\bar{u} \bar{v} \tan \phi / r$ , shading) and (b) convergence of eddy vertical momentum flux ( $-\rho^{-1} \partial(\rho \bar{u} \bar{w}) / \partial z$ , shading) in the experiment with topography and the differences in (c) the metric term and (d) convergence of eddy vertical momentum flux (shading) between Topo and Flat averaged over two Venus days, together with the difference in zonal flow (contours). The units of acceleration are  $\text{m s}^{-1} \text{Earth day}^{-1}$ . The gray dash line indicates the altitude of  $4.54 \times 10^3 \text{ Pa}$  ( $\sim 69 \text{ km}$ ). (For interpretation of the references to colour in this figure legend, the reader is referred to the web version of this article.)

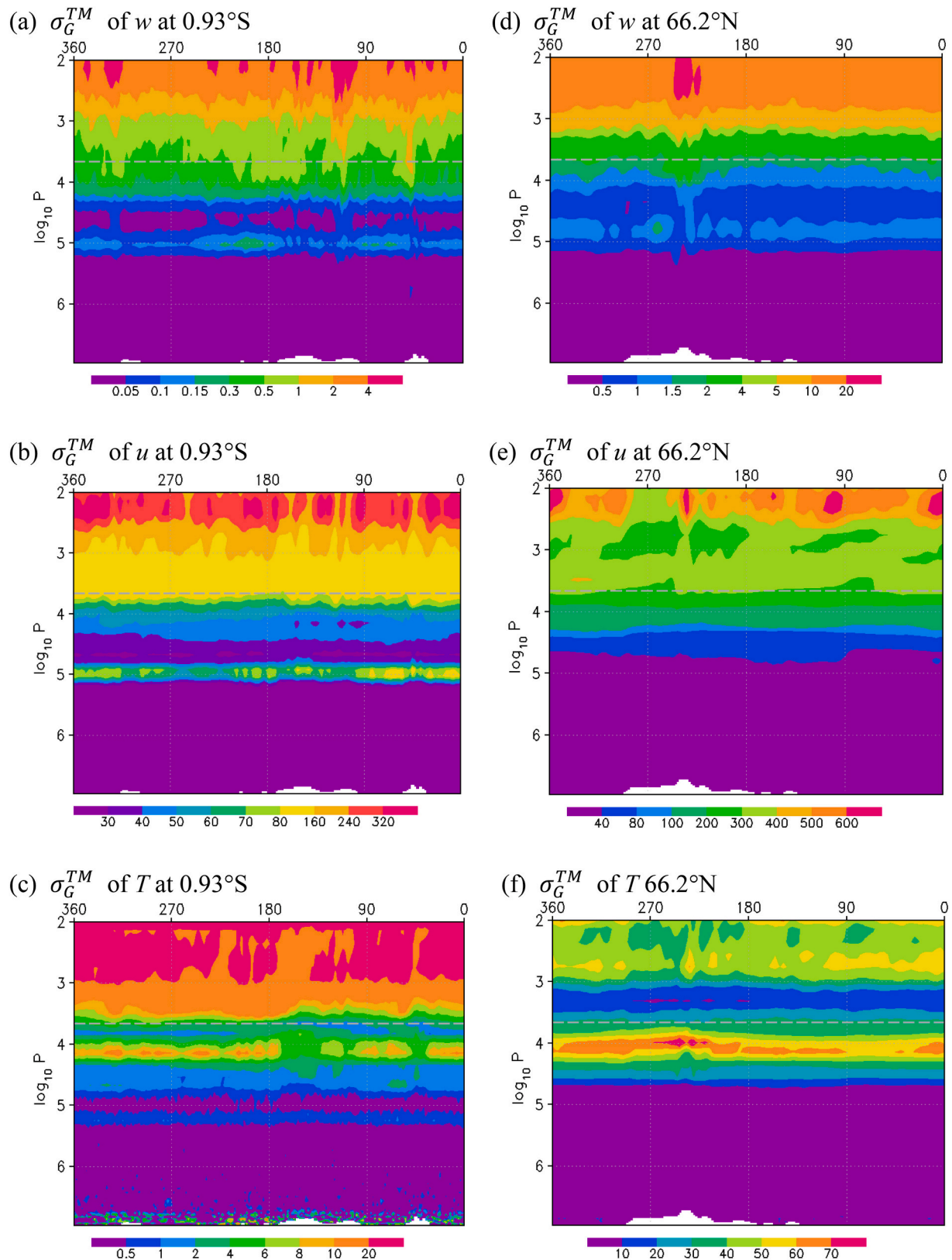
whereas the variance of zonal flow is not intensified by the high mountains in Fig. 12e.

At the cloud top ( $4.54 \times 10^3 \text{ Pa}$ ,  $\sim 69 \text{ km}$ ), there are zonal bands of variances (contours in Fig. 13a–d) at high latitudes. The variance of temperature in the Northern Hemisphere ( $\sim 30 \text{ K}^2$ , contours in Fig. 13a) is weaker than that in the Southern Hemisphere ( $\sim 40 \text{ K}^2$ ). The temperature variance is low above the Aphrodite Terra (blue and purple shading, denoting negative deviations in Fig. 13a) and low variances of meridional and zonal flows are located over the Aphrodite Terra (Fig. 13b and d). In contrast, the variances of vertical flow are locally enhanced over the Aphrodite Terra and Beta Regio ( $30^\circ \text{N}$  latitude,  $330^\circ$  longitude in geographical coordinates of our model) (positive shading in Fig. 13c). These variances are produced by locally-enhanced, fast waves with periods of  $< 10$  Earth days and small-scale (a few degrees) waves associated with the migration of solar heating in Fig. A2b (Appendix A). Over the Maxwell Montes, the variances of temperature and meridional flow are low, whereas the variance of vertical flow is high, though we cannot conclude whether these longitudinal variations are originated from the high mountains, or not.

Fig. 13e–h shows local-time variations of the variances at  $4.54 \times$

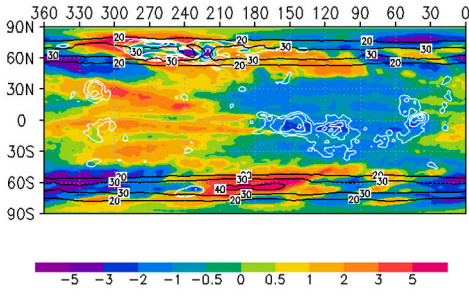
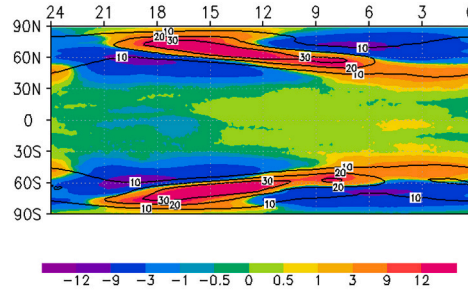
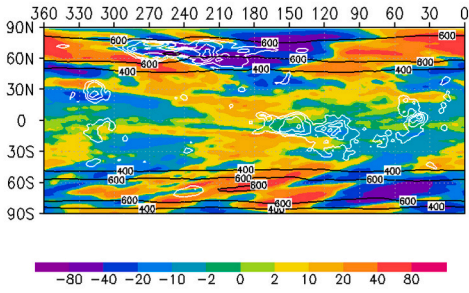
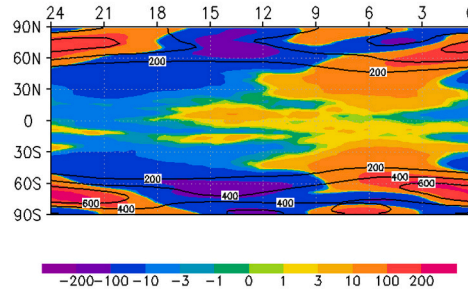
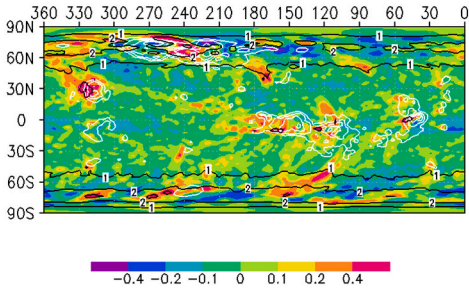
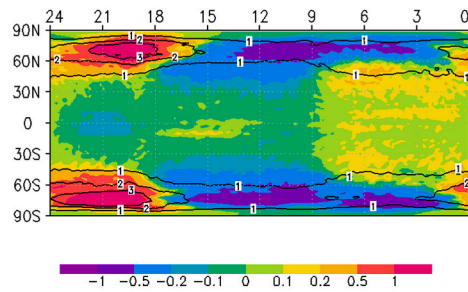
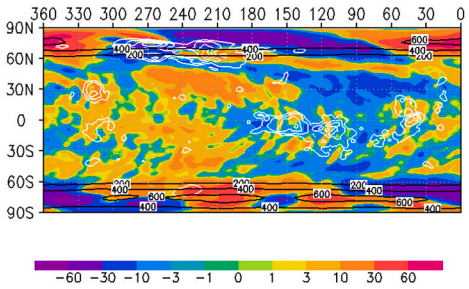
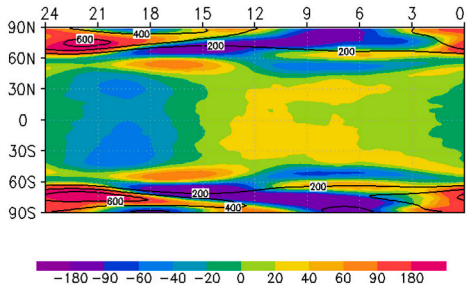
$10^3 \text{ Pa}$  ( $\sim 69 \text{ km}$ ). The variance  $\sigma_5^{TM}$  of time series data in the solar-fixed coordinates indicates the activity of waves excluding the time-mean thermal tides, as noted in Section 2.2. The local-time variations of the variances mean that waves other than the thermal tides are also modulated by solar heating. High variances (contours) are located in the areas of the strong polar tides between  $60^\circ$  and  $90^\circ$  latitude. At the mid- and low latitudes, the variances of  $T$ ,  $v$ , and  $u$  are relatively high in the region 0–12 LT and high variances of  $w$  are confined within 0–9 LT. Thus waves other than the thermal tides are active (the variances are high) in the local time zone from midnight to morning. This may support the results of Imamura et al. (2014), who found that convection and its associated waves are active in the nightside in a two-dimensional mesoscale model. The phase of these variances changes with increasing latitude around  $60^\circ$  latitude. At high latitudes, the variance of  $T$  is high on the dayside. In contrast, the variances of  $u$ ,  $v$ , and  $w$  are high from evening to midnight local time. The high variance of the vertical flow at 18–24 LT (at high latitudes of Fig. 13g) is produced by the local enhancements of fast waves in Fig. A3 (Appendix A).

A question still remains: what generates the spatial distributions of the variances in the geographical and solar-fixed coordinates? As



**Fig. 12.** Geographical longitude-pressure distributions of the variances calculated from time series data of (a, d) vertical wind, (b, e) zonal wind, and (c, f) air temperature at (a–c) 0.93°S and (d–f) 66.2°N latitude. The gray dash line indicates the altitude of  $4.54 \times 10^3$  Pa ( $\sim 69$  km). (For interpretation of the references to colour in this figure legend, the reader is referred to the web version of this article.)



(a)  $\sigma_G^{TM}$  of  $T$ (e)  $\sigma_S^{TM}$  of  $T$ (b)  $\sigma_G^{TM}$  of  $v$ (f)  $\sigma_S^{TM}$  of  $v$ (c)  $\sigma_G^{TM}$  of  $w$ (g)  $\sigma_S^{TM}$  of  $w$ (d)  $\sigma_G^{TM}$  of  $u$ (h)  $\sigma_S^{TM}$  of  $u$ 

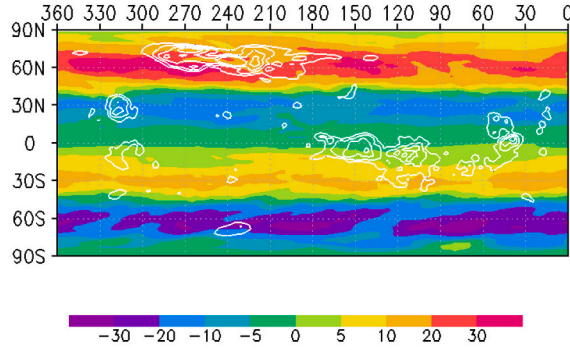
**Fig. 13.** Longitude-latitude distributions of the variances calculated from time-series data of (a, e) air temperature (K), (b, f) meridional wind ( $\text{m s}^{-1}$ ), (c, g) vertical wind ( $\text{mm s}^{-1}$ ) and (d, h) zonal wind ( $\text{m s}^{-1}$ ) at the cloud-top level of  $4.54 \times 10^3$  Pa ( $\sim 69$  km) in (a–d) geographical and (e–h) solar-fixed coordinates for two Venus days. Black contours and colour shading represent the variance and its deviation from the zonal mean, respectively. White contours (695, 705, and 715 K) indicate the lowermost-level temperature change that is modified by surface topography. (For interpretation of the references to colour in this figure legend, the reader is referred to the web version of this article.)

mentioned above, the small-scale gravity waves resolved in our model may generate a locally high variance. In addition, we must also consider spatiotemporal modulation of both the small-scale and large-scale waves seen in the time evolution of these snapshots. This new problem needs to be investigated in future wave analyses.

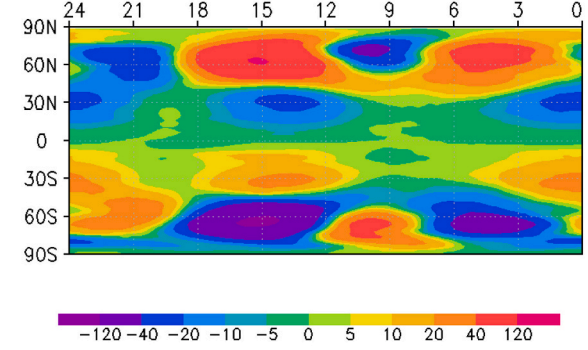
### 3.6. Longitudinal and local-time structures of eddy heat and momentum fluxes

The longitudinal structures of eddy heat and momentum fluxes in the geographical coordinates show whether eddy heat and momentum fluxes are locally modified by the surface topography. If longitudinal variations of the fluxes are highly correlated with the surface

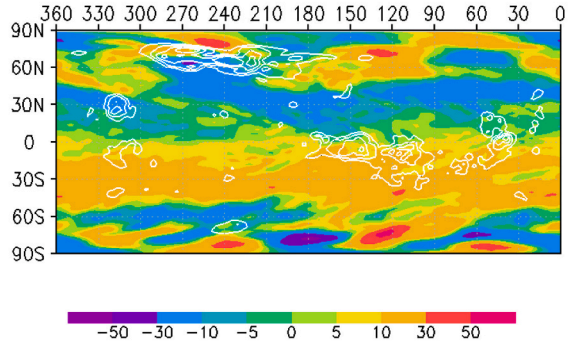
(a)  $(T_G'v_G')^{TM}$



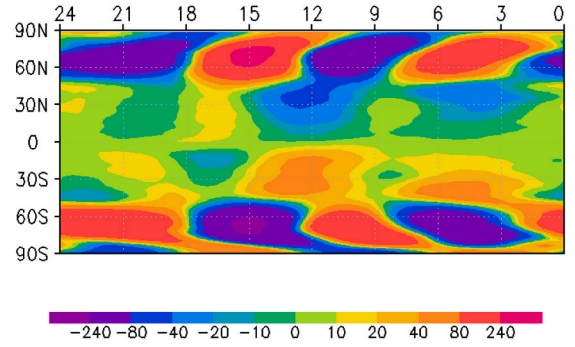
(d)  $(T_S'v_S')^{TM}$



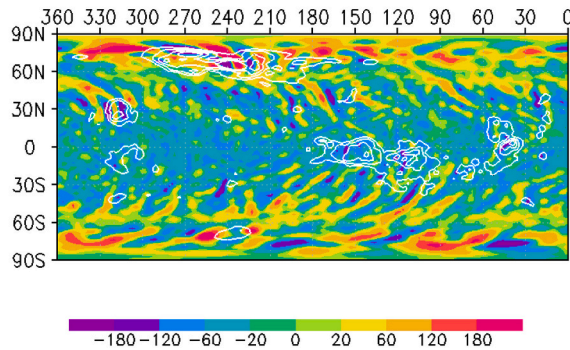
(b)  $(u_G'v_G')^{TM}$



(e)  $(u_S'v_S')^{TM}$



(c)  $(u_G'w_G')^{TM}$



(f)  $(u_S'w_S')^{TM}$

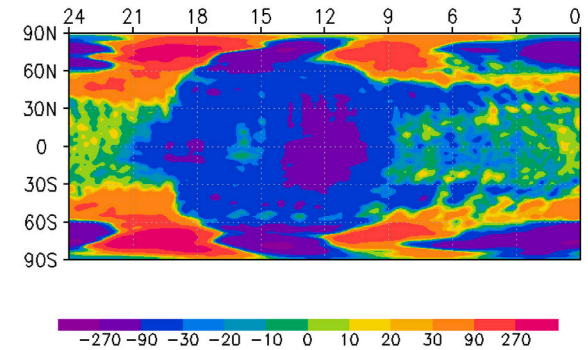


**Fig. 14.** Longitude-latitude distributions of (a, d) horizontal heat flux ( $\text{K m s}^{-1}$ ), (b, e) horizontal momentum flux ( $\text{m}^2 \text{s}^{-2}$ ) and (c, f) vertical momentum flux ( $\text{m}^2 \text{s}^{-2}$ ) of total waves, averaged over two Venus days at the cloud-top level of  $4.54 \times 10^3 \text{ Pa}$  in (a–c) geographical and (d–f) solar-fixed coordinates. White contours (695, 705, and 715 K) indicate the lowermost-level temperature change that is modified by surface topography. (For interpretation of the references to colour in this figure legend, the reader is referred to the web version of this article.)



topography, they are caused by the topography. If zonally traveling waves are independent of the surface topography, their fluxes are zonally uniform. Fig. 14a–c shows geographical longitude-latitude distributions of eddy heat and momentum fluxes at  $4.54 \times 10^3$  Pa ( $\sim 69$  km). The horizontal eddy heat flux is almost zonally uniform (Fig. 14a). However, the eddy heat flux locally decreases around the north of the Maxwell Montes and has the planetary-scale variations which are not correlated with the topography. The eddy horizontal momentum flux has a zonal wavenumber 2 structure and is enhanced at midlatitudes in the Northern Hemisphere (Fig. 14b) because the planetary-scale

stationary waves are formed over the Maxwell Montes in Fig. 8. This implies that the topography enhances the asymmetry of horizontal eddy momentum fluxes (blue curves in Fig. 4c and d). The horizontal eddy momentum fluxes have a high zonal wavenumber structure around the poles, where small-scale stationary eddies are predominant. The vertical eddy momentum flux has high zonal wavenumbers (Fig. 14c). In particular, fine-scale bow-shapes of strong negative fluxes are enhanced over the high mountains at low latitudes. The enhanced negative momentum fluxes might be associated with the locally slow zonal flow over the Aphrodite Terra (Bertaux et al., 2016; Yamamoto et al., 2019).

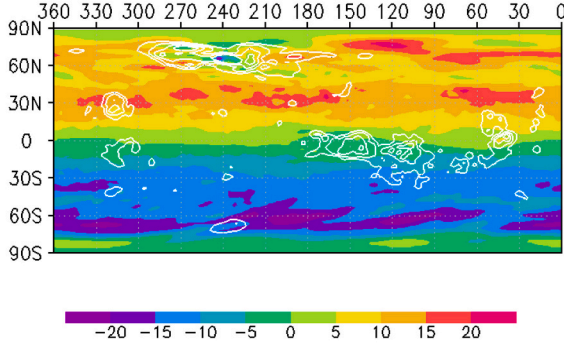
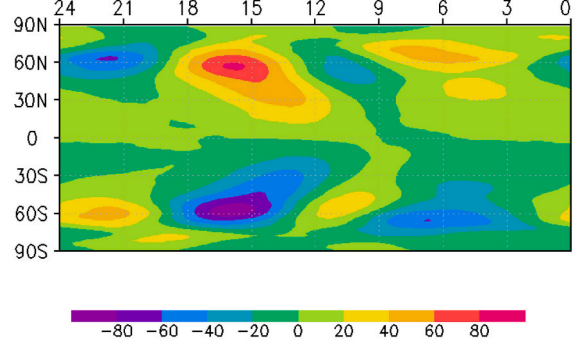
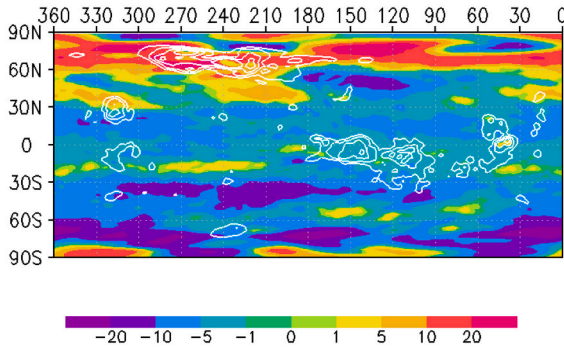
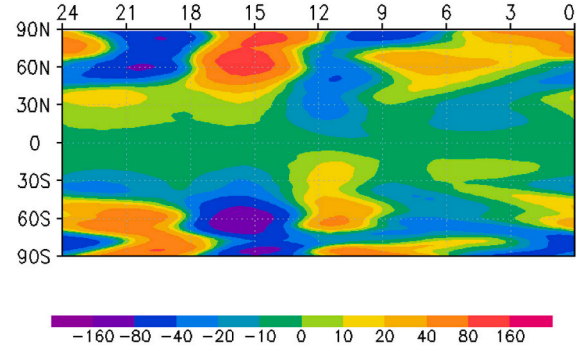
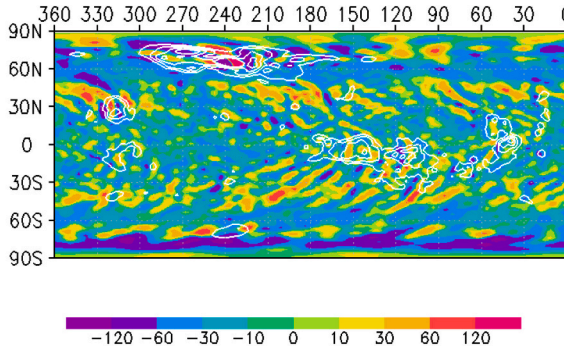
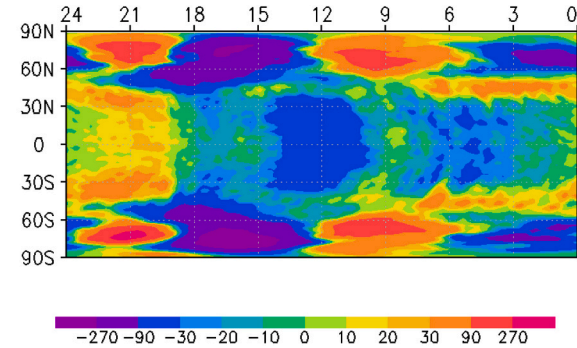
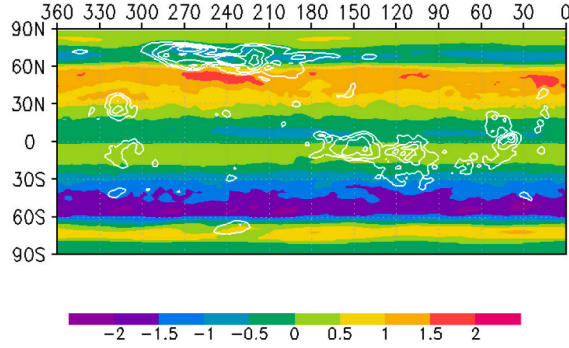
(a)  $(T_G'v_G')^{TM}$ (d)  $(T_S'v_S')^{TM}$ (b)  $(u_G'v_G')^{TM}$ (e)  $(u_S'v_S')^{TM}$ (c)  $(u_G'w_G')^{TM}$ (f)  $(u_S'w_S')^{TM}$ 

Fig. 15. As in Fig. 14, but for the cloud-heating maximum level of  $9.75 \times 10^3$  Pa.

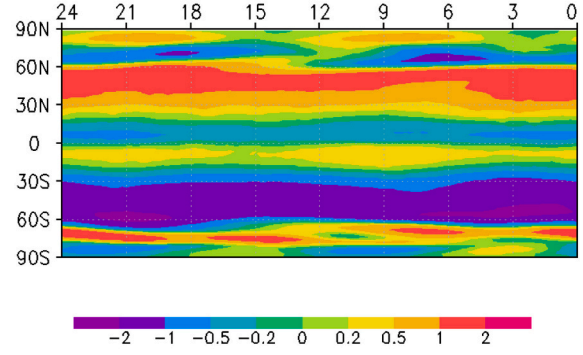
The local-time structures of eddy heat and momentum fluxes in the solar-fixed coordinates show whether the fluxes are modified by the solar heating. The local-time variations of the fluxes are produced by the thermal tides and gravity waves traveling with the solar heating. Fig. 14d–f shows local-time-latitude distributions of eddy heat and momentum fluxes at  $4.54 \times 10^3$  Pa ( $\sim 69$  km). Zonal wavenumber 2 components of eddy horizontal heat and momentum fluxes are produced by the poleward and equatorward flows of the diurnal tide (Fig. 14d and e). These flux magnitudes and directions vary strongly in the

longitudinal direction. Thus, as was discussed in Yamamoto et al. (2019), zonal-mean eddy momentum and heat fluxes averaged over the entire longitude range must be estimated carefully from those over the day- or night-side hemisphere. Vertical propagation of small-scale waves strongly depends on local time. Negative (downward) vertical momentum flux is found in the evening and noon areas (Fig. 14f). Positive (upward) vertical momentum flux is locally seen at 21–24 LT and 0–9 LT at low latitudes. The upward momentum flux is locally enhanced in the midnight and morning by small-scale gravity waves synchronized with

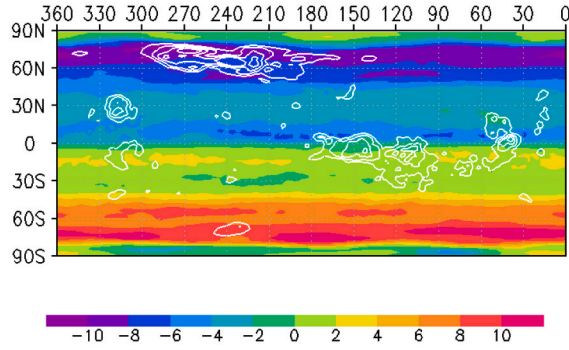
(a)  $(T_G'v_G')^{TM}$



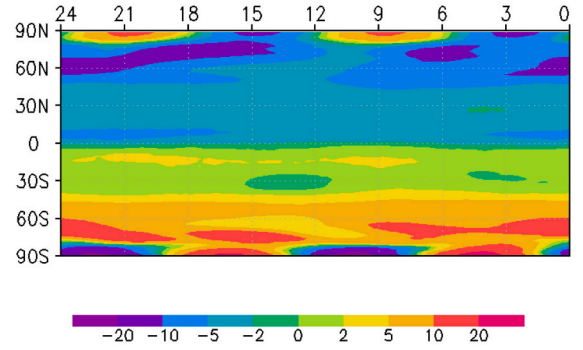
(d)  $(T_S'v_S')^{TM}$



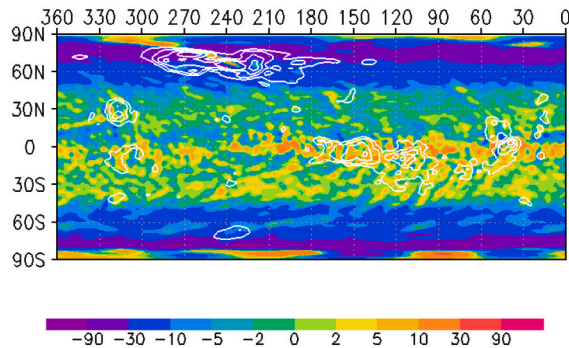
(b)  $(u_G'v_G')^{TM}$



(e)  $(u_S'v_S')^{TM}$



(c)  $(u_G'w_G')^{TM}$



(f)  $(u_S'w_S')^{TM}$

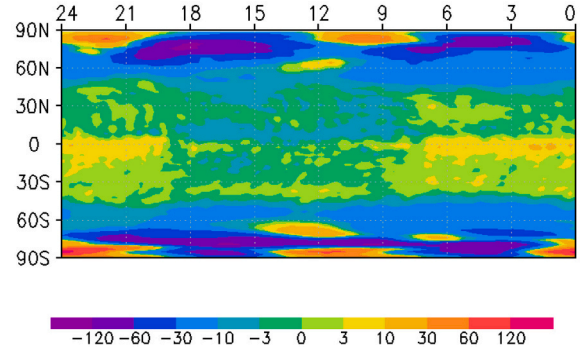


Fig. 16. As in Fig. 14, but for the altitude of  $1.38 \times 10^5$  Pa.



the migration of the solar heating.

At the cloud-heating maximum ( $9.75 \times 10^3$  Pa,  $\sim 65$  km) in the geographical coordinates, the horizontal heat flux is poleward for all the latitudes in Fig. 15a. The horizontal momentum flux is predominant at high latitudes in Fig. 15b. The vertical eddy momentum fluxes have bow shapes in Fig. 15c. Although the negative vertical eddy momentum flux over the high mountains at low latitudes is predominant at the cloud top in Fig. 14c, it is not seen at the cloud-heating maximum. In the solar-fixed coordinates, the poleward eddy heat flux is enhanced around 16 LT at  $9.75 \times 10^3$  Pa ( $\sim 65$  km) in Fig. 15d, while the horizontal eddy momentum flux is predominant at 12–24 LT. The downward eddy momentum fluxes are located around the subsolar point and morning terminator, whereas the upward fluxes are in 18–24 LT at low latitudes.

At  $1.38 \times 10^5$  Pa ( $\sim 48$  km, near the cloud base), the amplitudes of

the topographical waves and thermal tides are smaller than those around the cloud top. Thus, the horizontal heat and momentum fluxes are zonally uniform in the geographical and solar-locked coordinates, though there are longitudinal variations of the fluxes at high latitudes (Fig. 16a, b, d, and e). The topographical and local-time variations of the vertical momentum fluxes are small at low latitudes (Fig. 16c and f), compared to those at the cloud-top and cloud-heating maximum (Figs. 14 and 15).

### 3.7. Global structures of zonal-mean eddy heat and momentum fluxes

Fig. 17 shows latitude-pressure distributions of zonal-mean eddy heat and momentum fluxes (Eqs. 9–11) averaged over two Venus days, along with those of thermal tides (Eqs. 12–14) and stationary waves

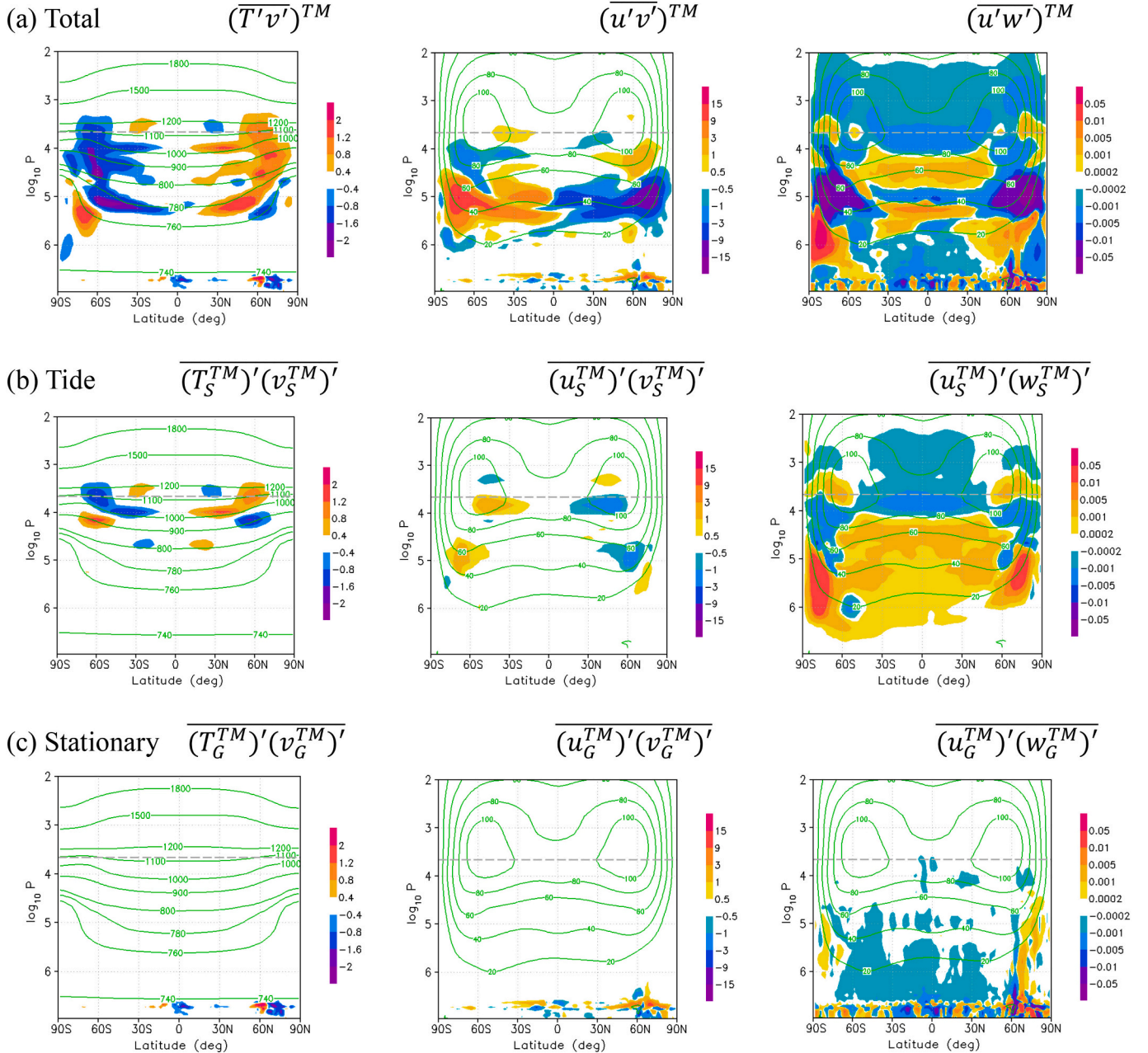


**Fig. 17.** Latitude–pressure distributions of zonal mean horizontal heat fluxes ( $\text{K m s}^{-1}$ , left column), horizontal momentum fluxes ( $\text{m}^2 \text{s}^{-2}$ , middle column), and vertical momentum fluxes ( $\text{m}^2 \text{s}^{-2}$ , right column) resulting from (a) total eddies, (b) tides and (c) stationary waves. The zonal-mean eddy fluxes (shading) are weighted by  $P/101,325$  (Pa). Green contours represent the potential temperature (K) in the left column and zonal wind speed ( $\text{m s}^{-1}$ ) in middle and right columns. The plotted quantities are averaged over two Venus days in the T63 experiment. The gray dash line indicates the altitude of  $4.54 \times 10^3$  Pa ( $\sim 69$  km). (For interpretation of the references to colour in this figure legend, the reader is referred to the web version of this article.)

(Eqs. 15–17). Poleward heat transport by total eddies is predominant in the regions where the horizontal gradient of potential temperature is high. Because the strongest poleward heat flux is predominant between  $3 \times 10^5$  and  $3 \times 10^3$  Pa (42 and 71 km), the indirect cells are also confined on the poleward flank of the jet core.

Equatorward momentum flux of total eddies is predominant around  $10^5$  Pa ( $\sim 50$  km). This supports the Gierasch–Rossow–Williams mechanism (Gierasch, 1975; Rossow and Williams, 1979). The eddy momentum flux is poleward around  $10^4$  Pa ( $\sim 65$  km) below the jet core, where the eddy heat flux is also poleward and the meridional gradient of the potential temperature is strong. Such poleward heat and momentum fluxes associated with high-latitude baroclinic waves (Yamamoto and Takahashi, 2016, 2018) were also reported in simplified models (Yamamoto and Tanaka, 1997; Sugimoto et al., 2014; Kashimura et al., 2019) and realistic GCMs (Lebonnois et al., 2016; Yamamoto et al., 2019). The horizontal eddy heat fluxes of total eddies are primarily produced by the thermal tides around the cloud top (gray dashed line on the left panels in Fig. 17a and b). The poleward heat and equatorward momentum fluxes of the tides are produced around the cloud-heating maximum.

The distribution of the eddy vertical momentum flux (the right panel of Fig. 17a) is complex. At low latitudes, the negative flux is seen above the cloud-heating maximum ( $<10^4$  Pa,  $>65$  km), in the low-stability layer ( $\sim 10^5$  Pa,  $\sim 50$  km), and below the  $10^6$ -Pa altitude ( $<30$  km). The sign of the strong vertical flux changes rapidly between  $10^6$  and  $10^4$  Pa (30 and 65 km) at high latitudes. In the right panel of Fig. 17b, the thermal tides produce the negative (positive) vertical momentum fluxes above (below) the cloud-heating maximum level at low- and mid-latitudes. As is shown in Fig. 6d, the semidiurnal tides propagate downward below the  $10^5$ -Pa altitude ( $\sim 50$  km) at  $70^\circ$  latitude. The downward propagating tides with phase velocity slower than the zonal flow generate positive vertical momentum flux between  $10^6$  and  $10^5$  Pa (30 and 50 km) on the poleward flank of the jet (the right panel of Fig. 17b).

As seen at  $66.2^\circ$ N in Fig. 9b, the stationary waves forced in the cloud layer propagate downward below the  $10^4$ -Pa altitude (65 km), where the vertical tilting of the stationary zonal-flow component is seen. In the right panel of Fig. 17c, the downward propagations of the stationary waves below the  $10^5$ -Pa altitude ( $\sim 50$  km) produce the positive vertical momentum flux near the poles in both hemispheres. However, the positive vertical momentum flux is enhanced over the Maxwell Montes near the northern pole, whereas it is small near the southern pole where there are no high mountains. This implies that polar high mountains influence the vertical propagation of stationary waves emitted from the cloud layer via standing wave or convection localized over the Maxwell Montes (Fig. 9b, d, and f).

In the region between  $10^6$  and  $10^5$  Pa, the eddy heat and momentum fluxes are generated by transient wave components obtained by removing tidal and stationary waves from the total wave components. In future work, we will elucidate the dynamics of the fast traveling eddies, which may produce the complex cloud features seen in the satellite-based observations.

#### 4. Concluding remarks

In our Venus GCM with long- and short-wave radiative processes, the increase in horizontal resolution greatly enhances the effect of the topography on the general circulation and stationary waves (Figs. 8 and 10) and better resolves the sharp streak structures of polar thermal tides (Fig. 2b and d). As in our previous low-resolution model, our simulation reproduces the UV-tracked horizontal flow around the subsolar point and the equatorial multi-layered and polar structures of static stability (Horinouchi et al., 2018; Ando et al., 2020). The simulated thermal tides are vertical and equatorward transporters of zonal momentum (Fig. 7a and Fig. 4c and d) around the cloud-heating maximum. The tidal accelerations are  $0.2\text{--}0.5 \text{ m s}^{-1} \text{ Earth day}^{-1}$  in Figs. 4e, f and 7c. In our model, the acceleration rate of the equatorward momentum flux of

thermal tides proposed by Yamamoto and Takahashi (2006) is of the same magnitude as that via the more conventional vertical momentum flux proposed by Fels and Lindzen (1974). Sharp streaks of vertical flow associated with polar thermal tides are located along the longitudinally extended trough and ridge at  $\sim 70^\circ$  latitude between the polar low and high in our T63 model (Fig. 2b and d). The radiative transfer forces diurnal and semidiurnal tides around the cloud top and also modifies the vertical structures of these waves and their momentum fluxes at multiple height levels (Fig. 7). The thermal tides accelerate not only equatorial zonal flow at the cloud-heating maximum ( $1 \times 10^4$  Pa,  $\sim 65$  km) but also the zonal flow around  $10^3$  Pa ( $\sim 75$  km) at low and high latitudes (Fig. 7c and d). Thus, we must consider the wind acceleration at various heights produced by thermal tides, when the super-rotation mechanism by thermal tides is discussed for each altitude.

Topographically locked fine-scale structures around the cloud top ( $\sim 69$  km) are revealed by our high-resolution model. Meridionally large-scale bow shapes of vertical flow with high zonal wavenumber are enhanced over the equatorial highlands (Fig. 8). Below and in the cloud layer, surface topography weakens the zonal-mean zonal flow over the Aphrodite Terra and Maxwell Montes, whereas it enhances the zonal flow in the southern polar region (Fig. 10). The convergence of eddy vertical momentum flux balances the metric term at high latitudes (Fig. 11a and b). The decrease in the metric term due to the topography produces the decrease/increase in the zonal flow at southern/northern high latitudes (Fig. 11c), which leads to the asymmetry of the zonal flow between the southern and northern polar regions.

Variances of time series are further investigated to assist in future comparisons with the observations. The variances are considered to result from unsteady eddy components in the geographical coordinates. The longitudinal variations of the wave activity are caused by surface topography and/or stationary waves. The vertical spikes in the vertical wind variance are striking around the equatorial high mountains (Fig. 12a), suggestive of penetrative plumes and vertically propagating gravity waves. At the cloud top, we also find bow shapes of negative vertical eddy momentum fluxes enhanced over the high mountains at low latitudes (Fig. 14c), where the zonal flow locally weakens over the Aphrodite Terra. In the solar-fixed coordinate system, the variances of flow are relatively higher on the nightside than on the dayside at low latitudes (Fig. 13e–h). The thermal tides produce strong dependences of the horizontal eddy heat and momentum fluxes on local time (Fig. 14d–e) and consequently lead to the difference between the zonal and dayside mean fluxes. The local-time variation of the vertical eddy momentum flux is produced by both thermal tides and solar-related, small-scale gravity waves at low latitudes (Fig. 14f).

The present work reveals the dynamical effects of high-resolution topographical and radiative forcings, based on the time-mean structures of waves (thermal tide and stationary waves) and variances using a high-resolution GCM with solar and infrared radiative transfer. Our future work will investigate fast waves with phase velocities almost the same as the superrotational wind speed, along with the observed cloud features.

#### Declaration of Competing Interest

None

#### Acknowledgments

This study was supported by a Grant-in-Aid for Scientific Research of Ministry of Education, Culture, Sports, Science, and Technology, Japan/Japan Society for the Promotion of Science (MEXT/JSPS KAKENHI Grant Number JP17H02960). The source code of the GCM was provided under the cooperative research activities for climate system research of the Atmosphere and Ocean Research Institute at the University of Tokyo, Japan. The data from the simulations are available upon request from the corresponding author.



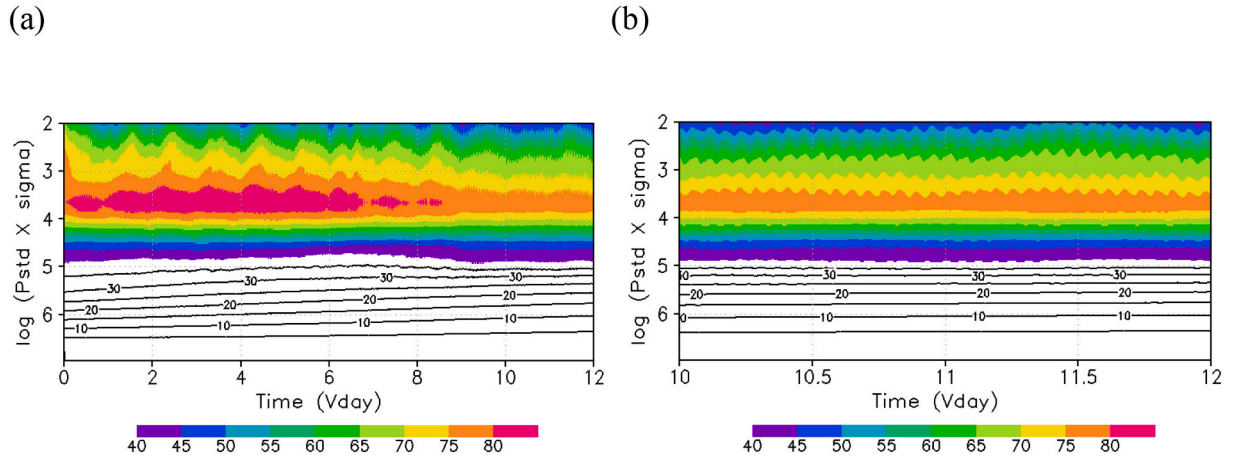
## Appendix A

### Time variations of angular momentum and vertical wind velocity

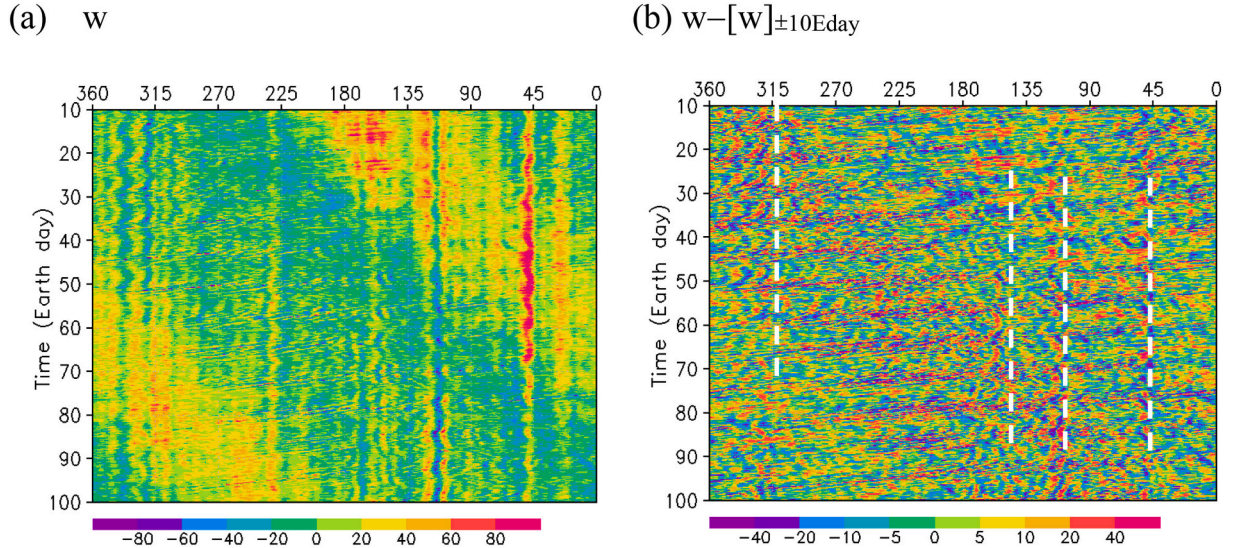
Fig. A1 shows the time histories of the global-mean specific relative angular momentum normalized by the planetary radius ( $\text{m s}^{-1}$ ). The angular momentum gradually varies over time in the T63 restart run (Fig. A1a) and does not largely change after Venus day 10. Because it is almost the quasi-equilibrium during Venus days 10 and 11 (Fig. A1b), we analyzed the GCM output in this period.

Fig. A2 shows the Hovmöller diagrams of vertical wind velocity at the equatorial cloud top ( $4.54 \times 10^3$  Pa and  $0.93^\circ\text{S}$  latitude) in the geographical coordinates. Large-scale stripes slowly travel with a 117-Earth day period and correspond to a diurnal tide. Stripes parallel to the time axis are formed by stationary waves with amplitudes that are strongly modulated by both the diurnal tides and fast waves (Fig. A2a). The short-period components are apparent on the stripes of the stationary waves (around white dashed lines in Fig. A2b). These fluctuations locally intensify the variance of the vertical flow in Fig. 12a. In addition, the enhancement area of small-scale (a few degrees in longitude) waves migrates with the solar heating area in Fig. A2b.

Fig. A3 shows the Hovmöller diagram of vertical wind velocity at the high-latitude cloud top ( $4.54 \times 10^3$  Pa and  $73.7^\circ\text{S}$  latitude) in the solar-fixed coordinates. The diurnal signals are positive around midnight (21–24 LT) and are negative around noon (12–15 LT). The fast waves with periods shorter than 10 Earth days are enhanced at 18–24 LT. Thus, the enhanced fast waves produce the high variance of the vertical flow at 18–24 LT at high latitudes in Fig. 13g.



**Fig. A1.** Time histories of the global-mean specific relative angular momentum normalized by the planet's radius ( $\text{m s}^{-1}$ ). (For interpretation of the references to colour in this figure legend, the reader is referred to the web version of this article.)



**Fig. A2.** Geographical longitude-time distributions of (a) vertical wind velocity component  $w$  ( $\text{mm s}^{-1}$ ) and (b) the vertical wind deviation ( $\text{mm s}^{-1}$ ) from the 20 Earth day running average between  $t-10$  Earth days and  $t+10$  Earth days for time  $t$  ( $w-[w]_{\pm 10\text{Eday}}$ ) at the cloud-top level of  $4.54 \times 10^3$  Pa and  $0.93^\circ\text{S}$  latitude. The time axis is labeled by Earth day from 00:00 on Venus day 10 in the restart T63 simulation. (For interpretation of the references to colour in this figure legend, the reader is referred to the web version of this article.)



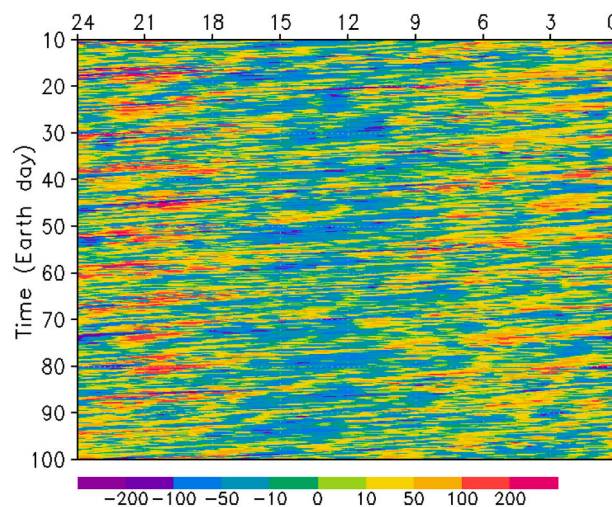


**Fig. A3.** Longitude-time distributions of vertical wind velocity component  $w$  ( $\text{mm s}^{-1}$ ) at the cloud-top level of  $4.54 \times 10^3$  Pa and  $73.7^\circ\text{S}$  latitude. The longitude is expressed by local time (LT) in the solar-fixed coordinates. The time axis is labeled by Earth day from 00:00 on Venus day 10 in the restart T63 simulation. (For interpretation of the references to colour in this figure legend, the reader is referred to the web version of this article.)

## References

- Ando, H., et al., 2018. Local time dependence of the thermal structure in the Venusian equatorial upper atmosphere: comparison of Akatsuki radio occultation measurements and GCM results. *J. Geophys. Res. Planets* 123, 2270–2280.
- Ando, H., et al., 2020. Thermal structure of the Venusian atmosphere from the sub-cloud region to the mesosphere as observed by radio occultation. *Sci. Rep.* 10, 3448.
- Bertaux, J.L., et al., 2016. Influence of Venus topography on the zonal wind and UV albedo at cloud top level: the role of stationary gravity waves. *J. Geophys. Res. Planets* 121, 1087–1101.
- Crisp, D., 1986. Radiative forcing of the Venus mesosphere. I - Solar fluxes and heating rates. *Icarus* 67, 484–514.
- Eymet, V., Fournier, R., Dufresne, J.-L., Lebonnois, S., Hourdin, F., Bullock, M.A., 2009. Net exchange parameterization of thermal infrared radiative transfer in Venus' atmosphere. *J. Geophys. Res.* 114, E11008.
- Fels, S.B., Lindzen, R.S., 1974. The interaction of thermally excited gravity waves with mean flows. *Geophys. Fluid Dyn.* 6, 149–191.
- Ford, P.G., Pettengill, G.H., 1992. Venus topography and kilometer-scale slopes. *J. Geophys. Res.* 97, 13103–13114.
- Fukuhara, T., et al., 2017. Large stationary gravity wave in the atmosphere of Venus. *Nat. Geosci.* 10, 85–88.
- Garate-Lopez, I., Lebonnois, S., 2018. Latitudinal variation of clouds' structure responsible for Venus' cold collar. *Icarus* 314, 1–11.
- Gierasch, P.J., 1975. Meridional circulation and the maintenance of the Venus atmosphere rotation. *J. Atmos. Sci.* 32, 1038–1044.
- Grassi, D., Migliorini, A., Montabone, L., Lebonnois, S., Cardesin-Moinelo, A., Piccioni, G., Drossart, P., Zasova, L.V., 2010. Thermal structure of Venusian nighttime mesosphere as observed by VIRTIS-Venus express. *J. Geophys. Res.* 115, E09007.
- Haynes, P.H., McIntyre, M.E., Shepherd, T.G., Marks, C.J., Shine, K.P., 1991. On the "downward control" of extratropical diabatic circulations by eddy-induced mean zonal forces. *J. Atmos. Sci.* 48, 651–678.
- Herrnstein, A., Dowling, T.E., 2007. Effects of topography on the spinup of a Venus atmospheric model. *J. Geophys. Res. Planets* 112, E04S08.
- Holton, J.R., 2004. *Introduction to Dynamic Meteorology*, 4th edition. Elsevier, Amsterdam, p. 535.
- Horinouchi, T., et al., 2018. Mean winds at the cloud top of Venus obtained from two-wavelength UV imaging by Akatsuki. *Earth Planets Space* 70, Article ID 10.
- Horinouchi, T., et al., 2020. How waves and turbulence maintain the super-rotation of Venus' atmosphere. *Science* 368, 405–409.
- Zasova, L.V., Khatuntsev, I.V., Ignatiev, N.I., Moroz, V.I., 2002. Local time variations of the middle atmosphere of Venus: solar-related structures. *Adv. Space Res.* 299, 243–248.
- Ignatiev, N.I., Titov, D.V., Piccioni, G., Drossart, P., Markiewicz, W.J., Cottini, V., Roatsch, Th., Almeida, M., Manoel, N., 2009. Altimetry of the Venus cloud tops from the Venus Express observations. *J. Geophys. Res.* 114, E00B43.
- Imamura, T., 1997. Momentum balance of the Venusian midlatitude mesosphere. *J. Geophys. Res.* 102, 6615–6620.
- Ikeda, K., 2011. Development of radiative transfer model for Venus atmosphere and simulation of superrotation using a general circulation model, Ph.D. thesis, The University of Tokyo, Japan.
- Imamura, T., et al., 2014. Inverse insolation dependence of Venus' cloud-level convection. *Icarus* 228, 181–188.
- Ingersoll, A.P., Crisp, D., Grossman, A.W., 1987. Estimates of convective heat fluxes and gravity wave amplitudes in the Venus middle cloud layer from VEGA balloon measurements. *Adv. Space Res.* 7, 343–349.
- K-1 model developers, 2004. In: Hasumi, H., Emori, S. (Eds.), K-1 Coupled GCM (MIROC) Description, K-1 Tech. Rep., 1. Center for Climate System Research, The University of Tokyo, Japan, p. 34.
- Kashimura, H., et al., 2019. Planetary-scale streak structure reproduced in high-resolution simulations of the Venus atmosphere with a low-stability layer. *Nat. Commun.* 10, 23.
- Kouyama, T., et al., 2017. Topographical and local time dependence of large stationary gravity waves observed at the cloud top of Venus. *Geophys. Res. Lett.* 44, 12098–12105.
- Kouyama, T., et al., 2019. Global structure of thermal tides in the upper cloud layer of Venus revealed by LIR on board Akatsuki. *Geophys. Res. Lett.* 46, 9457–9465.
- Lebonnois, S., Hourdin, F., Eymet, V., Cressin, A., Fournier, R., Forget, F., 2010. Superrotation of Venus' atmosphere analysed with a full general circulation model. *J. Geophys. Res. Planets* 115, E06006.
- Lebonnois, S., Eymet, V., Lee, C., Vatat d'Ollone, J., 2015. Analysis of the radiative budget of the Venusian atmosphere based on infrared net exchange rate formalism. *J. Geophys. Res. Planets* 120, 1186–1200.
- Lebonnois, S., Sugimoto, N., Gilli, G., 2016. Wave analysis in the atmosphere of Venus below 100-km altitude, simulated by the LMD Venus GCM. *Icarus* 278, 38–51.
- Lebonnois, S., Schubert, G., Forget, F., Spiga, A., 2018. Planetary boundary layer and slope winds on Venus. *Icarus* 314, 149–158.
- Lee, C., Richardson, M.I., 2011. A discrete ordinate, multiple scattering, Radiative transfer model of the Venus atmosphere from 0.1 to 260  $\mu\text{m}$ . *J. Atmos. Sci.* 68, 1323–1339.
- Lefèvre, M., Spiga, A., Lebonnois, S., 2020. Mesoscale modeling of Venus bow-shape waves. *Icarus* 335, Article ID 113376.
- Limaye, S.S., 1988. Venus: cloud level circulation during 1982 as determined from Pioneer cloud photopolarimeter images. II - solar longitude dependent circulation. *Icarus* 73, 212–226.
- Mendonça, J.M., Read, P.L., 2016. Exploring the Venus global super-rotation using a comprehensive general circulation model. *Planet. Space Sci.* 134, 1–18.
- Mendonça, J.M., Read, P.L., Wilson, C.F., Lee, C., 2015. A new fast and flexible radiative transfer method for Venus general circulation models. *Planet. Space Sci.* 105, 80–93.
- Navarro, T., Schubert, G., Lebonnois, S., 2018. Atmospheric mountain wave generation on Venus and its influence on the solid planet's rotation rate. *Nat. Geosci.* 11, 487–491.
- Newman, M., Leovy, C., 1992. Maintenance of strong rotational winds in Venus' middle atmosphere by thermal tides. *Science* 257, 647–650.
- Pechmann, J.B., Ingersoll, A.P., 1984. Thermal tides in the atmosphere of Venus: comparison of model results with observations. *J. Atmos. Sci.* 41, 3290–3313.
- Peralta, J., et al., 2017. Stationary waves and slowly moving features in the night upper clouds of Venus. *Nat. Astron.* 1, 0187.
- Rosow, W.B., Williams, G.P., 1979. Large-scale motion in the Venus stratosphere. *J. Atmos. Sci.* 36, 377–389.
- Sánchez-Lavega, A., Lebonnois, S., Imamura, R.P., Luz, D., 2017. The atmospheric dynamics of Venus. *Space Sci. Rev.* 212, 1541–1616.
- Scarica, P., et al., 2019. Validation of the IPSL Venus GCM thermal structure with Venus express data. *Atmosphere* 10, 584.

- Schofield, J.T., Taylor, F.W., 1983. Measurements of the mean, solar-fixed temperature and cloud structure of the middle atmosphere of Venus. *Q.J.R. Meteorol. Soc.* 109, 57–80.
- Smith, M.D., Gierasch, J., 1996. Global-scale winds at the Venus cloud-top inferred from cloud streak orientations. *Icarus* 123, 313–323.
- Sugimoto, N., Takagi, M., Matsuda, Y., 2014. Waves in a Venus general circulation model. *Geophys. Res. Lett.* 41, 7461–7467.
- Sugimoto, N., et al., 2017. Development of an ensemble Kalman filter data assimilation system for the Venusian atmosphere. *Sci. Rep.* 7, 9321.
- Takagi, M., Matsuda, Y., 2007. Effects of thermal tides on the Venus atmospheric superrotation. *J. Geophys. Res.* 112, D09112.
- Takagi, M., Sugimoto, N., Ando, H., Matsuda, Y., 2018. Three dimensional structures of thermal tides simulated by a Venus GCM. *J. Geophys. Res. Planets* 123, 335–352.
- Tellmann, S., Patzold, M., Hausler, B., Bird, M.K., Tyler, G.L., 2009. Structure of the Venus neutral atmosphere as observed by the Radio Science experiment VeRa on Venus Express. *J. Geophys. Res. Planets* 114, E00B36.
- Yamamoto, M., Takahashi, M., 2004. Dynamics of Venus' superrotation: the eddy momentum transport processes newly found in a GCM. *Geophys. Res. Lett.* 31, L09701 <https://doi.org/10.1029/2004GL019518>.
- Yamamoto, M., Takahashi, M., 2006. Superrotation maintained by meridional circulation and waves in a Venus-like AGCM. *J. Atmos. Sci.* 63, 3296–3314.
- Yamamoto, M., Takahashi, M., 2007. A parametric study of atmospheric superrotation on Venus-like planets: effects of oblique angle of planetary rotation axis. *Geophys. Res. Lett.* 34, L16202 <https://doi.org/10.1029/2007GL030220>.
- Yamamoto, M., Takahashi, M., 2009. Influences of Venus' topography on fully developed superrotation and near-surface flow. *Earth Planets Space* 61, e45–e48.
- Yamamoto, M., Takahashi, M., 2015. Dynamics of polar vortices at cloud top and base on Venus inferred from a general circulation model: case of a strong diurnal thermal tide. *Planet. Space Sci.* 113–114, 109–119.
- Yamamoto, M., Takahashi, M., 2016. General circulation driven by baroclinic forcing due to cloud-layer heating: significance of planetary rotation and polar eddy heat transport. *J. Geophys. Res. - Planets* 121, 558–573.
- Yamamoto, M., Takahashi, M., 2018. Effects of polar indirect circulation on superrotation and multiple equilibrium in long-term AGCM experiments with an idealized Venus-like forcing: sensitivity to horizontal resolution and initial condition. *J. Geophys. Res. - Planets* 123, 708–728.
- Yamamoto, M., Tanaka, H., 1997. Formation and maintenance of the 4-day circulation in the Venus middle atmosphere. *J. Atmos. Sci.* 54, 1472–1489.
- Yamamoto, M., Ikeda, K., Takahashi, M., Horinouchi, T., 2019. Solar-locked and geographical atmospheric structures inferred from a Venus general circulation model with radiative transfer. *Icarus* 321, 232–250.
- Yamazaki et al., 2018. Ultraviolet imager on Venus climate orbiter Akatsuki and its initial results. *Earth Planets Space* 70. Article ID 23.
- Young, R.E., Walterscheid, R.L., Schubert, G., Seiff, A., Linkin, V.M., Lipatov, A.N., 1987. Characteristics of gravity waves generated by surface topography on Venus: comparison with the VEGA balloon results. *J. Atmos. Sci.* 44, 2628–2639.
- Zasova, L.V., Ignatiev, N., Khatuntsev, I., Linkin, V., 2007. Structure of the Venus atmosphere. *Planet. Space Sci.* 55, 1712–1728.